Water Quality Monitoring of Roxo reservoir using Landsat Images and In-situ Measurements

Emmanuel Olet
March, 2010

Water Quality Monitoring of Roxo reservoir using Landsat Images and In-situ Measurements

by

Emmanuel Olet

Thesis submitted to the International Institute for Geo-Information Science and Earth Observation (ITC) in partial fulfilment of the requirements for the degree of Master of Science in Geo-information Science and Earth Observation, Specialisation: Environmental Hydrology

Thesis Assessment Board

Chairperson:	Prof. Dr. Ing. W. (Wouter) Verhoef	(ITC)
External Examiner:	Dr. M.A. (Marieke) Eleveld	(Vrije Universiteit, Amsterdam)
First Supervisor:	Dr. Ir. Mhd. (Suhyb) Salama	(ITC)
Second Supervisor:	Dr. Ir. C.M.M (Chris) Mannaerts	(ITC)
Advisor :	Mr. Syarif Budhiman	(ITC)

INTERNATIONAL INSTITUTE FOR GEO-INFORMATION SCIENCE AND EARTH OBSERVATION
ENSCHEDE, THE NETHERLANDS

Disclaimer

This document describes work undertaken as part of a programme of study at the International Institute for Geo-information Science and Earth Observation. All views and opinions expressed therein remain the sole responsibility of the author, and do not necessarily represent those of the institute.

Abstract

Water quality monitoring in fresh water bodies incorporating the use of earth observation products has become a major component in many a water quality monitoring program. This is majorly due to the inadequacies of traditional methods imposed by the lack of comprehensive and reliable in-situ datasets. In this study we explored the possibility to use Landsat imagery data to quantify pollutant indicators through estimation of water quality parameters of the Roxo reservoir waters. Chlorophyll-a (Chla) and suspended particulate matter (SPM) were the parameters of interest.

Landsat images for the Roxo reservoir acquired on 05-09-2000, 04-06-2001 and 01-07-2002 were obtained from the Landsat data archive. Owing to a lack of in-situ radiometric, Chla and SPM measurements on the Roxo reservoir, a dataset acquired on the Poyang Lake during a field excursion in October 2008 was incorporated in the study. The atmospheric correction algorithms and water quality models developed were trained on the Poyang Lake dataset and implemented on Roxo reservoir as a case study.

An image based atmospheric correction was implemented on the Landsat imagery data and validated using in-situ measured water leaving reflectance (WLR) on the Poyang Lake. The R^2 and RMSE values between the atmospherically corrected satellite derived WLR and in-situ measured values were 0.797 and 0.117 respectively.

Following a matrix inversion technique, a semi-analytical bio-optical model was used to estimate Chla, CDOM and SPM from atmospherically corrected WLR. However, this application yielded physically unrealistic estimates of Chla and SPM concentration. No analysis was done on CDOM due to a lack of CDOM in-situ measurements. The Area Chlorophyll-a Concentration Retrieved Model was then used to empirically estimate Chla, from which SPM was inferred. Chla concentrations derived were in the range 0.31 μgl^{-1} to 0.35 μgl^{-1} with R^2 = 0.295 and RMSE = 0.603μgl^{-1}. SPM concentrations on the other hand were in the range of 9 mgl^{-1} to 34 mgl^{-1} with an R^2=0.5 and RMSE =0.145 mgl^{-1} showing relatively high correlation between the satellite derived and in-situ measured concentrations of SPM.

This study has shown the possibility to implement image-based atmospheric correction on Landsat imagery and limitations of Landsat imagery for Chla and SPM retrieval using a semi-analytical bio-optical model. However, following an empirical approach Chla and SPM can still be derived. Landsat can, therefore, still play a critical role in water quality estimation for monitoring purposes on small inland lakes and other water bodies.

Keywords: water quality monitoring; remote sensing; Landsat; atmospheric correction; suspended particulate matters; Chlorophyll-a; Roxo reservoir

Acknowledgements

A number of people and organizations contributed immensely to the successful completion of this study.

I would like to thank the Royal Netherlands Government who funded this study through the Netherlands Fellowships Programme.

I am indebted to my employer, the Ministry of Water and Environment of Uganda, who through the Director of Water Resources Management and Commissioner of Water Resources Regulation allowed me to take up the opportunity to build my capacity through further training.

Many thanks go to Dr. Ir. Mhd. Suhyb Salama, who as my first supervisor provided expert guidance, support and continuous motivation throughout the entire study. I must also include Dr. Ir. Chris Mannaerts who as my second supervisor was always open to consultations granting me benefits of his vast knowledge and experience in the subject matter.

I would also like to register my appreciation to all staff in the Water Resources Department at the Faculty of Geo-Information Science and Earth Observation which was my home for the past few months. I will be eternally grateful for the experience and knowledge imparted through this brief association.

Lastly, I wish to acknowledge the unwavering moral support of my family and friends who contributed in one way or another to the successful completion of this study. Though it is not possible to mention them all, their assistance, nonetheless, is most sincerely appreciated.

May the Almighty God reward and bless you all abundantly.

Table of contents

List of figures

List of tables

List of symbols

Symbol	Description	Unit
a	bulk absorption coefficient	m^{-1}
a^*	specific absorption coefficient	m^{-1}
a_{dg}	bulk absorption coefficient of detritus	m^{-1}
a_{ph}	bulk absorption coefficient of phytoplankton	m^{-1}
a_w	bulk absorption coefficient of water molecules	m^{-1}
b_b	bulk backscattering coefficient	m^{-1}
b_w	backscattering coefficient of water molecules	m^{-1}
b_{spm}	backscattering coefficient of suspended sediment	m^{-1}
b^*	specific backscattering coefficient	m^2g^{-1}
l_1	coefficient	unitless
y	spectral slope of $b_{spm}(\lambda)$	unitless
γ	backscattering fraction	
s	spectral shape exponent	nm^{-1}
Q	ratio of up-welling radiance to up-welling irradiance	sr
Tr	air molecules transmittance	unitless
Ta	aerosol transmittance	unitless
Tv	diffuse atmospheric transmittance	unitless
$\eta_{(s,l)}$	ratio of water leaving reflectance at two wavelengths: *s* and *l*	unitless
α	Angstrom exponent of aerosol	unitless
$\varepsilon_{(s,l)}$	ratio of aerosol reflectance at two wavelengths: *s* and *l*	unitless
λ	wavelength	*n*m/μm
p_r	rayleigh scattering phase function	
Ψ	light scattering angle	radians
θo	sun zenith angle	radians
θv	satellite viewing angle	radians
Φo	sun azimuth angle	radians
Φv	satellite azimuth angle	radians
τ_r	rayleigh optical thickness	
τ_a	aerosol optical thickness	
t_{oz}	ozone atmospheric transmittance	
k	ozone absorption coefficient	
U	ozone total column content	cm-atm
ωa	single scattering albedo	unitless
z	altitude	m
$P(0)$	standard atmospheric pressure at sea level	mb
$P(z)$	atmospheric pressure at altitude z	mb
d	Earth-Sun distance	AU
π	Mathematical constant (3.14159)	unitless
$ESUN_\lambda$	Mean exoatmospheric solar irradiance	$Wm^{-2}\mu m^{-1}$
L_λ	spectral radiance at the sensor's aperture	$Wm^{-2}sr^{-1}\mu m^{-1}$
Qcal	quantized calibrated pixel value	DN
Qcalmin	minimum quantized calibrated pixel value corresponding to $LMIN_\lambda$	DN

Qcalmax	maximum quantized calibrated pixel value corresponding to $LMAX_\lambda$	DN
$LMIN_\lambda$	spectral radiance at the sensor scaled to Qcalmin	$Wm^{-2}sr^{-1}\mu m^{-1}$
$LMAX_\lambda$	spectral radiance at the sensor scaled to Qcalmax	$Wm^{-2}sr^{-1}\mu m^{-1}$
$L_a(\lambda)$	aerosol radiance	$Wm^{-2}sr^{-1}\mu m^{-1}$
$L_r(\lambda)$	rayleigh radiance	$Wm^{-2}sr^{-1}\mu m^{-1}$
$L_{sfc}(\lambda)$	surface radiance	$Wm^{-2}sr^{-1}\mu m^{-1}$
$L_t(\lambda)$	top of atmosphere radiance	$Wm^{-2}sr^{-1}\mu m^{-1}$
$L_w(\lambda)$	water leaving radiance	$Wm^{-2}sr^{-1}\mu m^{-1}$
ρ_λ	planetary TOA reflectance	unitless
$\rho_a(\lambda)$	aerosol reflectance	unitless
$\rho_c(\lambda)$	rayleigh corrected-reflectance	unitless
$\rho_r(\lambda)$	rayleigh reflectance	unitless
$\rho_{sfc}(\lambda)$	surface reflectance	unitless
$\rho_t(\lambda)$	total reflectance	unitless
$\rho_w(\lambda)$	water leaving reflectance	unitless

List of abbreviations

Term	Description
ACCRM	Area Chlorophyll-a Concentration Retrieved Model
AOP	Apparent optical properties
Chla	Chlorophyll-a pigment
CDOM	Coloured dissolved organic matters
EO	Earth observation
EROS	Earth Resources Observation and Science
ETM	Enhanced Thematic Mapper
GloVis	Global Visualisation Viewer
HCCRM	Height Chlorophyll-a Concentration Retrieved Model
ILWIS	Integrated Land and Water Information System
IOCCG	International Ocean Colour Coordinating Group
IOP	Inherent optical properties
NIR	Near-infrared
RMSE	Root mean of squared error
SeaWiFS	Sea-viewing Wide Field-of-view Sensor
SIOP	Specific inherent optical properties
SLC	Scan Line Corrector
SPM	Suspended particulate matters
TM	Thematic Mapper
TOA	Top of atmosphere
USGS	United States Geological Survey
WLR	Water leaving reflectance

1. Introduction

Land-based runoff into Roxo reservoir modulates the transportation of pollutants and affects, therefore, the quality of the water and human life use. The main source of pollutant loadings into the reservoir is therefore from non-point sources which are difficult to measure and quantify using traditional water quality measurement methods. Remote sensing therefore, offers the only realistic means of acquiring the required water quality measurements in the reservoir.

The lack of spatial and temporally representative water quality data is a genuine handicap in many water quality monitoring programs, thus the need to determine other methods to retrieve water quality parameters accurately. One of the ways to overcome this is to integrate earth observation products derived from satellite imagery in a management tool that may improve water quality monitoring and prediction (Shafique et al., 2001). Water management authorities are now able to develop multi-temporal algorithms for the estimation and retrieval of water quality variables (Östlund et al., 2001) from remote sensing data, in that satellite data can now be exploited as an independent water quality measurement, monitoring and management tool (Carpenter et al., 1983; Dekker et al., 2001; Lavery et al., 1993).

Landsat is cheap and has very long time series of archived data which can provide insight about historical events or developments in an area and can therefore be utilized for monitoring purposes. Previous studies show that Landsat has proven its capabilities to yield satisfactory results in lake water studies (Brivio et al., 2001; Lathrop, 1992). It has been the dominant source of satellite images for lake monitoring applications (Brivio et al., 2001; Lathrop et al., 1986; Mayo et al., 1995) and particularly in Europe (Baban, 1993; Dekker et al., 1993) owing to its spatial resolution of 30m ground pixel size.

(Dekker et al., 2001) were able to develop algorithms based on analytical modelling and minimum in-situ inherent optical properties to estimate water quality variables. This methodology enables the development of multi-temporal algorithms which can be employed by water management authorities to estimate dry seston weight concentrations in lakes from remote sensing data and as such, satellite data can now be relied upon as an independent measurement tool.

The quality of a water body is a key determinant in the usability of the resource depending on the purpose for which the water is required. It is therefore of great interest to managers of hydrologic resources to be able to confidently tell the quality status of the resource. This goes a long way in supporting the sustainable management of the resource.

1.1. Research problem

Roxo reservoir is the main source of water for both domestic and agricultural use in Beja.
In order for it to continue playing this role sustainably, it is of paramount importance that the quality of water in the reservoir doesn't deteriorate below acceptable standards. With increasing agricultural activities and human settlements within the area, the reservoir is threatened by increasing pollutant loadings that would in turn result in a continuous deterioration in the reservoir's water quality. For this to be assured, measures need to be put in place to monitor the quality of this water with deliberate interventions to ensure it does not deteriorate. An improvement in the reservoir's water quality monitoring and prediction would facilitate better management of this very important water source.

1.2. Research Objectives

The main objective of this study is to quantify pollutant indicators through estimation of water quality parameters indicative of deterioration in the quality of the Roxo reservoir waters based on Landsat images and in-situ measurements. But more specifically;

- Use/update an analytical model to derive water quality parameters for the Roxo reservoir from Landsat images
- Study the spatio-temporal variability of Roxo reservoir water quality

1.3. Research questions

1. Can Landsat images be used to derive water quality variables for Roxo reservoir using analytical algorithms?
2. Can Landsat imagery data be atmospherically corrected using an image-based case 2 water atmospheric correction algorithm?
3. What are the spatio-temporal characteristics (seasonal variability) of Roxo reservoir water quality?

1.4. Hypothesis

With an appropriate adaptation of an analytical model, a methodology can be developed for use in the Roxo reservoir to estimate water quality variables from Landsat imagery data**.**

Landsat imagery data can be used as an independent water quality measurement and monitoring tool on Roxo reservoir in lieu of in-situ measurements.

1.5. Structure of the thesis

This thesis outlines the results of a research undertaken to quantify water quality indicators on Roxo reservoir based on Landsat imagery products.

The report commences with an introduction (Chapter 1) that presents general background information on the study field, problem and also introduces the objectives of, and motivations for, the research. A review of the literature on water quality remote sensing and more specifically Landsat driven water quality estimation is presented in Chapter 2. Chapter 3 gives a brief description of the study area and the materials and datasets used in the study while 4 details the methodology applied in the execution of this study. The results of this study and their discussion are presented in Chapter 5. Chapter 6 contains the conclusions and recommendations.

2. Literature review

2.1. Water quality remote sensing

Conventional water quality monitoring requires elaborate in situ measurements and/or sequential laboratory analysis (Wang et al., 2004) which are extremely demanding in terms of time and capital investments. Traditional water quality monitoring methods, therefore, are not a viable and reliable option. This calls for the identification of other avenues through which this critical function can be performed. (Vignolo et al., 2006) advocate the integration of satellite remote sensing for water quality monitoring and assessment as a feasible option. With an improvement in sensor capabilities over the years,(Hakvoort et al., 2002) reveal that remote sensing has become an increasingly popular and promising technique in inland water quality monitoring programmes. This is due to the development of algorithms that can now accurately estimate water quality variables. (Kishino et al., 2005; Werdell et al., 2005) were able to relate broad band reflectance to other water column properties such as total suspended sediments, chlorophyll concentrations, pigment loads, temperature, secchi depth and other laboratory analysed water quality data with reasonable accuracy.

(Zilioli et al., 1997) demonstrate the suitability of satellite remote sensing observations as a fast and relatively low cost effective tool for early and expeditious assessment of both the spatial and temporal variability of lake water quality conditions.

In a comparative study to assess the ability of satellite based sensors to monitor suspended sediment concentration, secchi disk depth, and turbidity, (Harrington Jr et al., 1992) discovered that predictions based on optical measures of water quality, rather than measures of the weight of particles in the water column, are slightly better when using Landsat data.

2.1.1. Basis for water quality remote sensing

Radiative transfer theory provides the basis for water quality remote sensing. Incident solar radiation on a water surface is either absorbed or scattered back out of the water. The light scattered back is characterised by the absorption and scattering properties of all water constituents, including the water molecules (Mobley, 1994). The signal from water, often times referred to as ‘colour’, recorded at the sensor therefore contains information on water and its constituents. The water leaving signal, an apparent optical property (AOP) can be measured from space using earth observation sensors and is then related to water quality variables through the inherent optical properties (IOPs) of spectral absorption and scattering coefficients.

2.1.2. Atmospheric interferences

Radiation leaving the water surface is transmitted through the atmosphere and recorded at the sensor. However, this radiation undergoes a number of interferences such as scattering by atmospheric

constituents which include air molecules and dust particles and absorption and emission of radiation by the atmosphere's green house gases and water vapour (Mobley, 1994). These compromise the water leaving signal and must be accounted for.

Cloud cover provides the most significant impact of the atmosphere in remote sensing. Visible and near infra red (NIR) radiation do not penetrate clouds and would therefore render the registration of the water leaving signal by the sensor impossible. It is therefore important to ensure images are acquired in cloud free atmospheres since there is no way to correct for clouds.

Other than clouds, the rest of the atmospheric effects can be accounted for. A number of correction algorithms exist to improve quality of recorded water signal (Chomko et al., 2003; Gordon, 1997; Ruddick et al., 2000; Salama et al., 2004).

2.2. Semi-analytical models for water quality remote sensing

A number of semi-analytical models that link water leaving radiance to the IOPs of water have been developed. (Gordon et al., 1988) developed a semi-analytical model for surface water while (Lee et al., 1999) derived one for shallow waters.

All these models exploit hydro-optical properties to relate apparent optical properties to the inherent optical properties of water. For a uniform radiance field, the water leaving reflectance (WLR) can be linked to the IOPs through a function as (Gordon et al., 1975):

$$\rho_w(\lambda) \propto \frac{b_b(\lambda)}{b_b(\lambda) + a(\lambda)}$$

where $\rho_w(\lambda)$ is the WLR and $a(\lambda)$, $b_b(\lambda)$ are the bulk absorption and backscattering coefficients of the water column respectively. These IOPs are related to the types and concentrations of dissolved and suspended water constituents which are majorly; chlorophyll-a, detritus and dissolved organic matter (dg) and suspended particulate matter (SPM).
The concentrations of the water quality parameters can then be derived from the IOPs through the specific inherent properties (SIOPs) following the Lambert-Beer law.

2.3. Adaptation of the Gordon reflectance bio-optical model for water quality retrieval

The Gordon model was used to relate the IOPs to the observed WLR as:

$$\rho_w(\lambda) = 0.54 l_1 Q \frac{b_b(\lambda)}{b_b(\lambda) + a(\lambda)}$$

where l_1 is a constant coefficient; Q is the ratio between upwelling radiance and irradiance (Mobley, 1994) and the constant number 0.54 describes the fraction of transmitted light from below the water surface.

Originally designed for use in open ocean applications with high spectral and low spatial resolution satellite data, this model has been adapted to cater for the high spatial and low spectral resolution characteristics of Landsat data for use in non-coastal water. It should be noted however, that the Gordon reflectance model does not perform very well in highly absorbing and backscattering situations (IOCCG, 2006) which is characteristic of Case 2 inland waters.

This adaptation yielded a semi analytical model that was inverted to derive concentrations of Chla, CDOM and SPM as retrievable variables.

2.4. The Empirical determination of water quality variables

An empirical model based on the geometric characteristics of the triangle between reflectance in the three Landsat visible bands was used to derive Chlorophyll-a concentrations.

This was achieved by exploiting the spectral geometric triangle properties of water leaving reflectance derived from Landsat satellite data (Figure 2-1). Previous studies such as (Shrestha et al., 2005; Walsh et al., 2008) utilised the same spectral absorbing features for applications on land. The shape of the triangle would be deformed as a result of the different reflectances from phytoplankton pigments at the different wavelengths leading to variances in height, area and angle of the triangle. Nonetheless, (Chen et al., 2009) show a high correlation between these geometric quantities of the triangle ABC with Chla concentration.

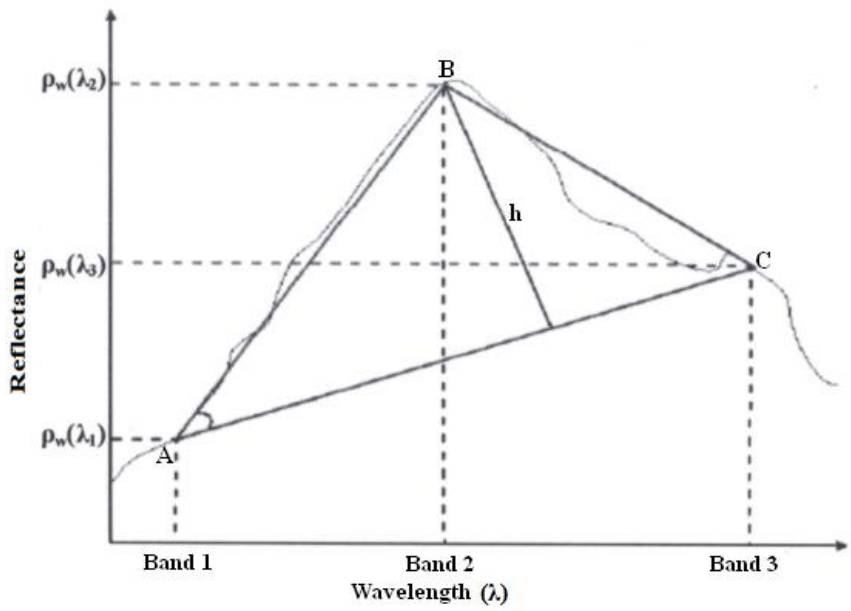

Figure 2-1: Triangular properties between the three Landsat visible bands and reflectance; h is height of the triangle ABC with baseline AC

(Chen et al., 2009) investigated the applicability of three empirical models based on height, area and angle of the triangle in the turbid waters of Taihu Lake, China and found a high exponential correlation between Chla concentration and the geometric properties of height (R^2=0.8023) and area(R^2=0.7985) and very low correlation with the angle(R^2=0.0001). The Height Chlorophyll-a

Concentration Retrieved Model (HCCRM) and the Area Chlorophyll-a Concentration Retrieved Model (ACCRM) were found to be suitable for Chla mapping in the Taihu Lake. However, both models overestimated the concentration of Chla with a total bias in estimation of -3.570 μgl^{-1} for HCCRM and -4.003$\mu gl^{-1}$for ACCRM.

2.5. Landsat driven water quality retrieval

The first four bands of Landsat are in the visible and near infra red spectral range where light passes through water and is therefore able to provide some water quality information (Giardino et al., 2001; Kloiber et al., 2002). A number of studies have been able to exploit these bands to retrieve water quality parameters such as suspended matter, dissolved organic matter, chlorophyll-a, phytoplankton to mention but a few (Dekker et al., 1993; Giardino et al., 2001; Jacquet et al., 1989; Kloiber et al., 2002; Lathrop et al., 1986; Onderka et al., 2008; Pattiaratchi et al., 1994) with satisfactory results.

(Dekker et al., 1993) show that TM1 can be used to measure the irradiance attenuation due to the absorption of aquatic humus and chlorophyll-a; TM2 can be used to determine phytoplankton concentrations, TM3 though difficult to interpret due to the large number of counter-acting processes which affect it can provide useful information on sediment loads, and TM4 reflectance can reveal information on water absorption and, probably, suspended matter reflection.

Table 2-1: Spectral characteristics of Landsat TM and Landsat ETM+ bands significant for water quality studies

Band	Sensor	Spectral range (μm)	Applications
Blue (1)	TM ETM	0.452-0.518 0.452-0.514	Absorption by aquatic humus and Chla. Towards 0.5μm, absorption decreases, leading to increasing reflectance
Green (2)	TM ETM	0.528-0.609 0.519-0.601	Mixture between absorption due to dissolved organic matter and increasing reflectance due to SPM backscattering
Red (3)	TM ETM	0.626-0.693 0.631-0.692	Small reflectance peak at 0.645μm followed by strong absorption due to Chla at 0.665μm Generally, reduction in upwelling radiance due to absorption counteracted by scattering
NIR (4)	TM ETM	0.776-0.904 0.772-0.898	High absorption by water in 0.850-0.900μm. important for atmospheric correction

(Source: http://landsathandbook.gsfc.nasa.gov/handbook/handbook_toc.html)

With atmospheric effects a major setback in the utilization of satellite imagery, (Brivio et al., 2001) applied image based correction models that required no in-situ measurements during satellite overpass with satisfactory results. With a root mean square error between Landsat TM derived reflectance and ground measurements close to 0.010 for each TM spectral band, this approach constitutes a valid method of lake water monitoring.

Using an empirical approach to relate Landsat TM data to in-situ measurements of several water quality parameters including chlorophyll-a and suspended solids, (Baban, 1993) was able to consistently predict and map these parameters.

Due to the high spatial and temporal variability of water quality, a methodology that is just as versatile was developed by (Dekker et al., 2002) to be able to track the spatio-temporal variations in lake water quality. Using minimum in-situ inherent optical properties, algorithms based on analytical modelling were developed to estimate water quality variables. This methodology enables the development of multi-temporal and multi-site algorithms which can be employed by water management authorities to estimate dry seston weight concentrations in lakes from remote sensing data and as such, satellite data can now be relied upon as an independent measurement and monitoring tool.

3. Study area and Materials

3.1. Description of Study areas

This study was executed using two different sites; Roxo reservoir in Portugal and the Poyang Lake in China. The methodology developed during the research was implemented on both sites with the Poyang Lake serving the purpose of calibration and validation of the models. This is due to the more comprehensive dataset of field measurements on Chlorophyll-a (Chla) and Suspended Particulate Matter (SPM) available for this lake. Following the developed methodology, the trained model was then implemented on the Roxo reservoir.

3.1.1. General description of Roxo reservoir, Portugal

Located in the Portuguese municipality of Aljustrel and specifically in the district of Beja, Roxo reservoir is the principal source of water for both domestic and agricultural use in the region. It was built between 1963 to1968, about 400m downstream of a confluence of rivers at Monte Salto to support agricultural activities in the region by providing water in good quality and quantity for irrigation and domestic use.

The geographical location of the dam is 37º55’48’’ N and 8º6’9’ W and supplies a total irrigated area of 5041 ha and is shown in Figure 3-1 below.

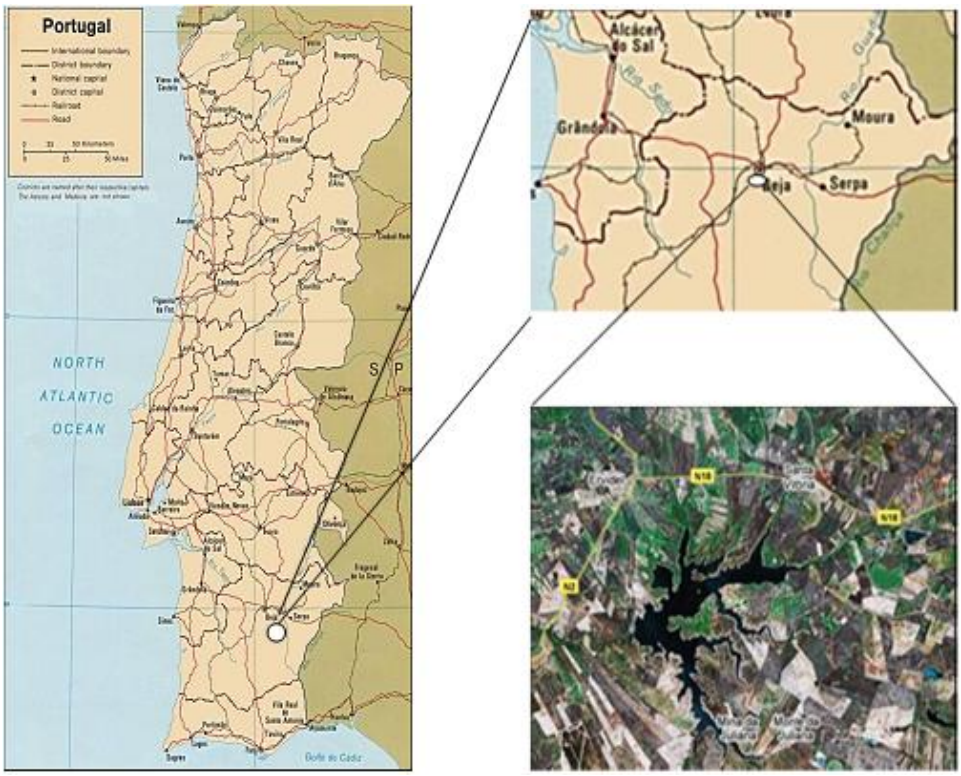

Figure 3-1: Location of Roxo reservoir in Portugal (left) and Roxo reservoir (bottom right)
Sources: (http://www.travel-images.com/portugal-map.jpg; http.www.maps.google.com)

3.1.2. General description of Poyang Lake, China

Located in the northern part of Jiangxi province, the Poyang Lake is the largest freshwater lake in China. The geographical location of the Lake is 29º09' N and 116º13' E and is shown in Figure 3-2 below.

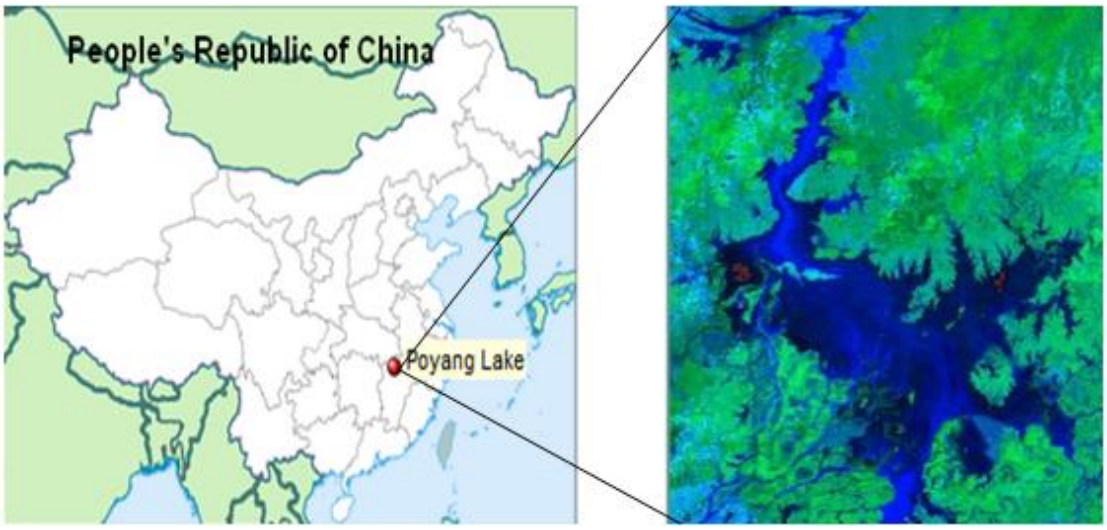

Figure 3-2: Location of Poyang Lake on the map of China (left) and the Poyang Lake (right)
Source: (http://en.wikipedia.org/wiki/Poyang_Lake)

Table 3-1: Main hydrological and morphological parameters of Poyang Lake

Parameter	Value (or names)
Elevation (a.m.s.l.)	12 m
Lake surface area	4400 km^2 (rainy season)
	1000 km^2 (dry season)
Water Volume	2.95 km^3
Mean depth	8.4 m
Maximum depth	25.1 m
Maximum length	170 km
Maximum width	17 km
Residence time	5000 years
Out flowing river:	Yangtze (through a channel)
Major inflowing rivers:	Gan, Xiu, Xin, Fu, Rao

With a catchment area of 162, 225 km^2, Poyang Lake supports directly or indirectly the livelihoods of more than 8 million people that live in its catchment. The Lake is a natural habitat to diverse species of plants, birds, animals and fish. The main economic activity is sand dredging which is negatively impacting on the Lake. It is also relied upon for food (fish), transport, tourism, recreation and as pollution sink for waste disposal. This Lake is also a major source of water for domestic use. However, over the years, the quality of the lake's waters has been deteriorating with pollution, flooding, erosion, degradation and eutrophication as its major environmental concerns. This was as a result of unsustainable exploitation of its resources and other anthropogenic activities in the catchment majorly sand dredging.

Deliberate protective measures were taken by the Government of China and this lake has since 1992 been declared a Ramsar site.
(http://www.globalnature.org/docs/02_vorlage.asp?id=15793&sp=E&m1=11089&m2=11093&m3=11178&m4=15621&m5=15793&m6=&domid=1011 (accessed 31/12/2209))

3.2. Description of Study Materials used

3.2.1. In-situ data

Owing to lack of in-situ measurements of Chla and SPM concentrations on the Roxo reservoir, this study co-opted the Poyang Lake in China to test the validity of the methodology employed. A substantial amount of in-situ measurements from the Poyang Lake were readily available from previous studies as is expanded on here under.

Following a field campaign carried out in the Poyang Lake in China during 2008 by (Zhou, 2009), in-situ measurements of Chla and SPM concentrations were carried out in 30 sites during the period between 15th to 19th October 2008. An ocean optics protocol (Fargion et al., 2000) was employed in the estimation of SPM and Chla concentration from the collected water samples.

Summarily, water samples were collected and filtered. The filters were then analysed for their content of SPM and Chla from the residue there on.

Table 3-2 below gives a statistical summary of the measured values of SPM and chlorophyll-a determined from the collected water samples from the Poyang Lake.

Table 3-2: Statistical summary of measured concentrations of chlorophyll-a (Chla) and SPM in the Poyang Lake

Location	Parameter	Nr .samples	Range	Mean	Standard deviation
Poyang Lake	SPM (gm^{-3})	30	13 - 36	25	7.13
	Chla (μgm^{-3})	30	0.152 -5.412	1.059	1.071

The locations of these sites and the measured concentrations of Chla and SPM are shown in Table 3-3.

Table 3-3: Locations of the sampling sites and measured values of Chla and SPM concentrations

Site	Coordinate		Measured concentrations	
	Lat	Long	Chla (μgm^{-3})	SPM (mgm^{-3})
P1	29.256567	116.073833	0.229	27
P2	29.246567	116.088567	1.416	19
P3	29.237550	116.101217	1.695	13
P4	29.228417	116.125317	0.808	13
P5	29.219300	116.152683	1.809	19
P6	29.209767	116.189550	3.495	14
P7	29.200828	116.191000	0.430	13
P8	29.191683	116.191683	0.933	32
P9	29.184417	116.197833	5.412	29
P10	29.175733	116.200150	1.430	31
P11	29.188967	116.210167	1.384	35
P12	29.199683	116.214944	1.730	18
P13	29.209400	116.212083	0.305	26
P14	29.221167	116.190883	0.344	24
P15	29.221128	116.200767	0.387	29
P16	29.392600	116.029367	1.193	32
P17	29.383617	116.041483	0.657	21
P18	29.374467	116.052883	1.012	31
P19	29.366050	116.059617	0.301	30
P20	29.356167	116.063850	0.152	25
P21	29.346167	116.063833	0.577	36
P22	29.337433	116.062450	0.428	16
P23	29.333767	116.059283	0.215	36
P24	29.320117	116.055050	0.711	31
P25	29.310400	116.051500	1.189	22
P26	29.301167	116.048583	0.806	28
P27	29.291983	116.048067	0.808	28
P28	29.282967	116.054050	0.999	17
P29	29.274000	116.058017	0.385	26
P30	29.265133	116.062100	0.534	26

In addition to these measurements, concurrent field measurements of water leaving reflectances (WLR) were also obtained from Poyang Lake (Table A3) during the same campaign using an ASD Spectrometer.

The in-situ measurements were used in the calibration and validation of the algorithms employed in the implementation of atmospheric correction and retrieval of water quality parameters.

(Zhou, 2009) provides a detailed description of the procedures used and the data collected during this field campaign.

3.2.2. Earth Observation (EO) data set

A series of Landsat images of the study area were downloaded from the Landsat imagery archive. This data archive is hosted by the United States Geological Survey (USGS) Earth Resources Observation and Science (EROS) Centre and is readily accessible and freely available on the internet. The Landsat scenes were downloaded using the USGS Globalisation Visualisation Viewer (GloVis) tool available at (http://glovis.usgs.gov/).

Three scenes of the Roxo reservoir acquired on September 5th, 2000; June 4th, 2001 and July 1st, 2002 and a single scene of the Poyang Lake in China acquired on October 15th 2008 were downloaded from the archive.

The Landsat scenes used in this study are from both the Landsat Thematic Mapper (TM) onboard the Landsat 5 platform and the Enhanced Thematic Mapper (ETM) onboard Landsat 7. Both platforms are at an altitude of 705 km with the sensors at an inclination angle of 98.2 degrees (Chander et al., 2009).

With a spatial resolution of 30m for the six reflective bands and 120m for the thermal bands, the TM sensor which belongs to the second generation of Landsat satellites marked a significant advance in remote sensing through the addition of a more sophisticated sensor, improved acquisition, transmission and processing of data.

The Landsat 7 ETM sensor on the other hand, belongs to the third generation of Landsat satellites. It has a spatial resolution of 30m for the six reflective bands, 60m for the thermal band and also includes a panchromatic (pan) band with a 15m resolution.

The TM images are acquired in low-gain state while ETM images are acquired in either low or high-gain state. These gain settings are used to ensure maximum utilisation of the sensors 8-bit radiometric resolution whilst avoiding saturation of the detectors. The low gain mode is used to image bright surfaces while the high gain mode is used to image surfaces with low brightness.

One critical observation for the image acquired for Poyang Lake from the ETM sensor is that it has got data gaps. This is because the image was acquired after the failure of the Scan Line Corrector (SLC) which occurred on May 31st, 2003. The SLC used to ensure all scans were aligned parallel to each other by compensating for the forward motion of the spacecraft. According to (Storey et al., 2005), approximately 22% of a normal scene area is lost due to the malfunction of the SLC mirror. It should be noted though that this anomaly has no bearing on the radiometric performance with the valid pixels. Much as there are procedures to correct for this anomaly, no attempt was made to do so. This is owing to the fact that the proposed procedures follow a methodology where a second scene acquired at a different time is used to fill the data gaps through linear histogram matching. This would

therefore compromise the products from the image since the image acquisition date wouldn't match the field measurement date.

The above description about Landsat data was summarised from the Landsat Science Date User's Handbook and information accessed from the Landsat website http://landsat.gsfc.nasa.gov/

A summary of the satellite imagery and field measured data used in this study with their acquisition dates, platform and sensor for the EO data and parameters measured for the field data are shown in Table 3-4.

Table 3-4: Summary of earth observation and field measured data used in the study

A: Satellite data

A1: Roxo reservoir, Portugal

No.	Date acquired	Platform	Sensor	WRS Path/Row	Cloud cover
1.	September 5th, 2000	Landsat	ETM	203/033	0%
2.	June 4th, 2001	Landsat	ETM	203/033	0%
3.	July 1st, 2002	Landsat	TM	203/033	0%

A2: Poyang Lake, China

1.	October 15th, 2008	Landsat	ETM	121/040	0%

B: Field measurements

Station	Date	Parameter measured
Poyang Lake		
30 in-situ points (Table 3-2)	15th -19th /Oct/2008	Chla, SPM, WLR

3.2.3. In-situ and EO data match-ups

Match-up site is a field measurement and an image pixel value at the same geographical location. These match-ups were used in the calibration and validation of the algorithms developed. Following the SLC anomaly, there were gaps in the final image products from the Poyang Lake. 10 field

measurement sites were located in these data gaps leading to a reduction in the number of valid match up sites to 20.

3.2.4. Auxiliary data

The total ozone column content, *U* and the ozone absorption coefficient, *k* were obtained from http://jwocky.gsfc.nasa.gov/ and from (Neckel et al., 1981) respectively.

Data on the atmospheric pressure at each location was calculated using the Air Map software that required the location's altitude as input.

4. Methodology

4.1. Landsat Imagery processing

4.1.1. Imagery acquisition and pre-processing

The different Landsat scenes were downloaded from the USGS Landsat archive using the USGS Globalisation Visualisation Viewer (GloVis) tool via a File transfer protocol (FTP) as Level 1T products.

Level IT processed Landsat data products are stored in an HDF file format and have the following properties:

- Pixel Size – 30 for the Visible and NIR/SWIR spectral range
- Map projection – UTM
- Ellipsoid - WGS84
- Image orientation - North up
- Output format - GeoTIFF

The downloads were then extracted as GeoTIFF files with scenes containing separate image files for each of the 8 bands, a metadata file and ground control points file.
Bands 1 to 4 were then imported into ILWIS software. This was achieved using the file menu option Import via GDAL as import format option. This converted the GeoTIFF image files into ILWIS raster maps. Sub maps of the study area were then created and the images were now ready for further processing and analysis.

4.1.2. Conversion of raw DNs to spectral radiance at the sensor (Qcal to L_λ)

Level IT Landsat data products are distributed as calibrated digital numbers (Q_{cal}). In order to obtain spectral radiance (L_λ) recorded at the sensor, a conversion of the recorded signal is required. This conversion (Q_{cal} to L_λ) can be obtained by using the equation (Chander et al., 2009):

$$L_\lambda = \left[\frac{LMAX_\lambda - LMIN_\lambda}{Qcal\max - Qcal\min}\right](Qcal - Qcal\min) + LMIN_\lambda \quad (1)$$

where

L_λ= Spectral radiance at the sensor's aperture [W/ (m^2srμm)]
Qcal= Quantized calibrated pixel value [DN]
Qcalmin= Minimum quantized calibrated pixel value corresponding to $LMIN_\lambda$ [DN]
Qcalmax= Maximum quantized calibrated pixel value corresponding to $LMAX_\lambda$ [DN]
$LMIN_\lambda$= Spectral radiance at the sensor scaled to Qcalmin [W/ (m^2srμm)]
$LMAX_\lambda$= Spectral radiance at the sensor scaled to Qcalmax [W/ (m^2srμm)]

4.1.3. Conversion of radiance to TOA reflectance (L_λ- to ρ_λ)

Top of the atmosphere (TOA) reflectance recorded at the sensor is obtained by converting the radiance recorded at the sensor to reflectance using the equation (Chander et al., 2009):

$$\rho_\lambda = \frac{\pi * L_{\lambda *} d^2}{ESUN_{\lambda *} \cos(\theta o)} \quad (2)$$

where

ρ_λ = Planetary TOA reflectance [unitless]

π = Mathematical constant (3.14159) [unitless]

L_λ = Spectral radiance at the sensor's aperture [W/ (m^2srμm)]

d = Earth-Sun distance [astronomical units]

$ESUN_\lambda$ = Mean exoatmospheric solar irradiance [W/m^2μm]

Θo = Solar zenith angle [degrees]

For each image, theses values were taken from Landsat calibration files (Table A1) and the image metadata (Table A2) shown in Appendices.

4.2. Atmospheric Correction of Landsat Imagery data

In order to derive any meaningful information from satellite data, the signal recorded at the sensor needs to be corrected for atmospheric effects. This is because the radiance recorded at the sensor is from different sources in addition to the water leaving reflectance. The fraction of radiance reflected from water column is very small, usually less than 20% of total signal, and therefore accurate radiometric correction is critical(Gordon, 1997).

The total radiance received at the sensor at the top of the atmosphere (L_t) can be divided into several components as:

$$L_t(\lambda) = L_r(\lambda) + L_a(\lambda) + T_v(\lambda)(L_{sfc}(\lambda) + L_w(\lambda)) \quad (3)$$

where L_r is radiance resulting from scattering by air molecules(Rayleigh scattering) in the absence of aerosols, L_a is the contribution from aerosol scattering in the absence of air, L_{sfc} is the contribution from the surface, T_v is the viewing diffuse transmittance of the atmosphere and L_w is the desired water leaving radiance.

It follows therefore, by conversion of radiance to reflectance; the total reflectance $\rho_t(\lambda)$ recorded at the sensor can be divided into the following components:

$$\rho_t(\lambda) = \rho_r(\lambda) + \rho_a(\lambda) + Tv(\lambda)(\rho_{sfc}(\lambda) + \rho_w(\lambda)) \quad (4)$$

where the subscripts of the reflectance represent the contribution from air molecules *r*, aerosol *a*, surface *sfc*, and water *w*.

$\rho_{sfc}(\lambda)$ is considered very small and is henceforth dropped (low wind speeds assumed) leaving:

$$\rho_t(\lambda) = \rho_r(\lambda) + \rho_a(\lambda) + Tv(\lambda)\rho_w(\lambda)) \tag{5}$$

The water leaving reflectance (WLR) $\rho_w(\lambda)$ can be extracted from total received reflectance at the sensor by carrying out atmospheric correction.

4.2.1. Rayleigh reflectance estimation

In terms of geometry and pressure (Gordon et al., 1988), the contribution of Rayleigh scattering to the total reflectance can accurately be obtained as described below:

$$\rho_r(\lambda) = \frac{t_{oz}\tau_r p_r}{4\cos(\theta o)\cos(\theta v)} \tag{6}$$

where p_r is the Rayleigh scattering phase function. The Rayleigh (molecular) scattering phase function is obtained from its relationship with the scattering angle which is described by the following expression:

$$p_r = 0.75\left(1 + Cos^2\Psi\right) \tag{7}$$

where Ψ is the light scattering angle. From sensor viewing and illumination geometry, this angle is well described by (Mobley, 1994) as:

$$Cos\Psi = Cos\theta oCos\theta v + Sin\theta oSin\theta vCos(\Phi o - \Phi v) \tag{8}$$

where θo, θv are sun zenith and satellite viewing angles and Φo, Φv the sun and satellite azimuth angles in radians, respectively.

τ_r is Rayleigh optical thickness, calculated as (Hansen et al., 1974)

$$\tau_r(\lambda, z) = 0.008569\lambda^{-4}\left(1 + 0.0113\lambda^{-2} + 0.00013\lambda^{-4}\right)\frac{P(z)}{P(0)} \tag{9}$$

where λ is wavelength in μm and *P(0)=1013.25 mb* is standard atmospheric pressure at sea level. z is altitude. $P(z)$ is atmospheric pressure at altitude z that is obtained from a solution of pressure-elevation relationship.

t_{oz} is two way ozone atmospheric transmittance given by (Viollier et al., 1980) as:

$$t_{oz} = \exp\left(-k(\lambda)U(\cos^{-1}(\theta o) + \cos^{-1}(\theta v)\right) \quad (10)$$

where $k(\lambda)$ is the ozone absorption coefficient from (Neckel et al., 1981) and U is the ozone total column content in cm-atm, obtained from http://jwocky.gsfc.nasa.gov/

These values are wavelength dependent and were therefore determined for each of the Landsat spectral bands.

4.2.2. Aerosol scattering reflectance determination

Assuming water leaving reflectance in the Near Infrared (NIR) band is zero, $\rho_w(\lambda_4) = 0$ leaves total reflectance in band 4 consisting of only the aerosol and Rayleigh reflectance components:

$$\rho_t(\lambda_4) = \rho_r(\lambda_4) + \rho_a(\lambda_4) \quad (11)$$

Having estimated Rayleigh reflectance for band 4, aerosol reflectance can then be obtained from the Rayleigh corrected reflectance as.

$$\rho_a(\lambda_4) = \rho_t(\lambda_4) - \rho_r(\lambda_4)$$

However, the determination of aerosol reflectance requires that the wavelength dependence of aerosol reflectance and the spatial and temporal variability of the spectral behaviour and size distribution of the aerosol particles be taken into account. The spectral dependence of aerosol scattering reflectance can be approximated as:

$$\rho_a(\lambda) = \rho_a(\lambda_o)\left(\frac{\lambda}{\lambda_o}\right)^{-\alpha} \quad (12)$$

where α is the Angstrom exponent and λ_o, a reference wavelength. The Angstrom exponent was obtained from the epsilon value for aerosol correction derived from Landsat ETM+ bands 3 and 4 at wavelengths of 0.662μm and 0.835μm respectively. This is a calibration parameter that was determined for each image.

According to (Ruddick et al., 2000), the epsilon value can be determined from the aerosol multiple-scattering ratio at two wavelengths (short and long) taken as band 3 and 4 respectively for Landsat, using the relation:

$$\varepsilon_{(s,l)} = \frac{\rho_a(\lambda_3)}{\rho_a(\lambda_4)} \quad (13)$$

This was quantified according to (Salama et al., 2004) as:

$$\varepsilon_{(s,l)} = Cot\left[0.5\tan^{-1}\left(\frac{C_{LL}}{C_{SS} - C_{SL}}\right)\right] \quad (14)$$

where C is the correlation between Rayleigh corrected reflectances in which the values in the short and long wavelength are denoted by the subscripts S and L respectively.
Combining equations (12), (13) and (14) yields the relation:

$$\varepsilon_{(s,l)} = \left(\frac{\lambda_3}{\lambda_4}\right)^{-\alpha} \tag{15}$$

From which α was then obtained as:

$$\alpha = -\left(\frac{In\varepsilon_{s,l}}{In\left(\frac{\lambda_3}{\lambda_4}\right)}\right) \tag{16}$$

Assuming a rural aerosol model over the entire study area for the entire day, the value obtained for each image was taken as being spatially homogeneous over the entire study area.

This is then extrapolated to determine aerosol reflectance in the other 3 bands by implementing equation (12).

4.2.3. Water leaving reflectance (WLR) determination

Following equation (5), water leaving reflectance was determined as:

$$\rho_w(\lambda) = (\rho_t(\lambda) - \rho_r(\lambda) - \rho_a(\lambda))/Tv(\lambda) \tag{17}$$

The viewing diffuse transmittance, *Tv* is determined as a product of the two-way diffuse atmospheric transmittances of air molecules and aerosol particles represented as *Tr* and *Ta* respectively as shown in the equation below:

$$Tv(\lambda, z) = Tr(\lambda, z)Ta(\lambda, z) \tag{18}$$

The aerosol transmittance *Ta* can be calculated as:

$$Ta(\lambda, z) = \exp\left[-\frac{(1-\omega a(\lambda)F(\lambda))\tau a(\lambda)}{\cos(\theta)}\right] \tag{19}$$

where $F(\lambda)$ is the ratio of the forward scattering to the scattering coefficient. The terms $\omega a(\lambda)$ and $\tau a(\lambda)$ are the single scattering albedo and the optical thickness of aerosol respectively.

However, this study approximated the value of $Ta(\lambda, z)$ as unity following (Gordon et al., 1987).

According to (Viollier et al., 1980), *Tr* is then determined as:

$$Tr = \frac{\left[\left(1+\exp(-\pi r Cos^{-1}\theta v\right)\left(1+\exp(-\pi r Cos^{-1}\theta o\right)\right]}{4} \quad (20)$$

This is in effect taken as *Tv* since *Ta* =1.

Having obtained values for *Tv*, an implementation of equation (17) yielded water leaving reflectances in the different spectral bands.

4.3. Adaptation of the Atmospheric Correction algorithm for turbid waters

For turbid waters, an implementation of the proposed atmospheric algorithm which is designed for clear water, yields physically unrealistic negative reflectances in the visible bands. The failure of the atmospheric correction can be attributed to an over estimation of the aerosol reflectances.

Turbid water is easily identified by an inspection of the top of the atmosphere radiances in the near infrared bands which turn out to be relatively high. The failure of the atmospheric correction therefore, can be attributed to the assumption adopted earlier in the estimation of aerosol reflectance that water leaving radiances in the near infra red bands is zero.

With this in mind, an adaptation of the atmospheric correction to suit turbid water is aimed at primarily estimating a more accurate reflectance due to aerosols. It therefore, follows the same procedure up to the estimation of aerosol reflectance. To overcome the error resulting from the assumption of zero values for water leaving reflectance in the near infra red bands, the following new assumptions were made to yield two relations that were used in the process.

First, the ratio of reflectance due to the multi-scattering aerosols for bands 3 and 4 of Landsat $\varepsilon_{(s,l)}$ were assumed to be spatially homogenous over the study area (equation 13).

Secondly, the ratio of water leaving reflectances in bands 3 and 4 were also assumed to be spatially homogeneous over the study area. According to (Carder et al., 1999), this ratio is:

$$\eta(s,l) = \frac{\rho_w(\lambda_3)}{\rho_w(\lambda_4)} \quad (21)$$

Following (Gordon et al., 1975), WLR $\rho_w(\lambda)$, can be linked to the water inherent optical properties (IOPs) after correcting for the air-water interface interaction as:

$$\rho_w(\lambda) = 0.54 l_1 Q \frac{b_b(\lambda)}{b_b(\lambda) + a(\lambda)} \quad (22)$$

where l_1= 0.0949 is a constant coefficient; and $a(\lambda)$, $b_b(\lambda)$ are the bulk absorption and backscattering coefficients of the water column respectively. Q is the ratio between upwelling radiance and irradiance (Mobley, 1994). Assuming an isotropic light field, the value of Q is taken as equal to π

(3.142) sr. The constant number 0.54 describes the fraction of transmitted light from below the water surface.

The above equation therefore holds true for surface layer of water, a nadir viewing angle, negligible internal reflection and a uniform radiance field in the water body.

Assuming absorption due to coloured dissolved organic matter (CDOM), phytoplankton- related pigments and other suspended particulate matter are negligible compared to absorption by pure water, $a_w(\lambda)$ in the near infrared bands which for this study and the case of Landsat are bands 3 and 4:

$$a(\lambda) = a_w(\lambda) \tag{23}$$

And also, assuming the bulk backscattering coefficient is independent of wavelength for the NIR wavelength ranges under consideration yields:

$$b_b(\lambda) = b_{bo} \tag{24}$$

Rewriting equation (23) for bands 3 and 4 of Landsat gives the expressions:

$$\rho_w(\lambda_3) = 0.54 l_1 Q \frac{b_{bo}}{b_{bo} + a_w(\lambda_3)} \tag{25}$$

$$\rho_w(\lambda_4) = 0.54 l_1 Q \frac{b_{bo}}{b_{bo} + a_w(\lambda_4)} \tag{26}$$

The ratio of the WLR is therefore determined by combining the above equations as:

$$\eta_{(s,l)} = \frac{\rho_w(\lambda_3)}{\rho_w(\lambda_4)} = \frac{b_{bo} + a_w(\lambda_4)}{b_{bo} + a_w(\lambda_3)} \tag{27}$$

The values of $\eta_{(s,l)}$ are estimated from in situ measurements as explained in (Ruddick et al., 2000)

For the Landsat bands of interest, reflectance due to aerosol $\rho_a(\lambda)$ can be estimated as:

$$\rho_c(\lambda) = \rho_a(\lambda) + T_v(\lambda)\rho_w(\lambda) \tag{28}$$

where $\rho_c(\lambda)$ is Rayleigh corrected reflectance, and $Tv(\lambda)$ is known from viewing geometry and choice of aerosol model as described earlier.

Writing equation (28) for bands 3 and 4 give:

$$\rho_c(\lambda_3) = \rho_a(\lambda_3) + Tv(\lambda_3)\rho_w(\lambda_3)) \tag{29}$$

$$\rho_c(\lambda_4) = \rho_a(\lambda_4) + Tv(\lambda_4)\rho_w(\lambda_4)) \tag{30}$$

From equation (13), aerosol scattering reflectance in band 3 is:

$$\rho_a(\lambda_3) = \varepsilon_{(s,l)}\rho a(\lambda_4) \tag{31}$$

and from equation (21), WLR in band 3 is:

$$\rho_w(\lambda_3) = \eta(s,l)\rho_w(\lambda_4) \tag{32}$$

Using equations (31) and (32), equation (29) can therefore be rewritten as:

$$\rho_c(\lambda_3) = \varepsilon_{(s,l)}\rho_a(\lambda_4) + \eta(s,l)Tv(\lambda_4)\rho_w(\lambda_4) \tag{33}$$

It follows therefore, from equation (30) that TOA WLR in band 4 is:

$$Tv(\lambda_4)\rho_w(\lambda_4)) = \rho_c(\lambda_4) - \rho_a(\lambda_4) \tag{34}$$

Substituting for WLR in equation (33) gives:

$$\rho_c(\lambda_3) = \varepsilon_{(s,l)}\rho_a(\lambda_4) + \eta(s,l)\left[\rho_c(\lambda_4) - \rho_a(\lambda_4)\right] \tag{35}$$

Expanding the equation and subsequently collecting like terms:

$$\rho_c(\lambda_3) = \left(\varepsilon_{(s,l)} - \eta(s,l)\right)\rho_a(\lambda_4) + \eta(s,l)\rho_c(\lambda_4) \tag{36}$$

Making $\rho_a(\lambda_4)$ the subject:

$$\left(\varepsilon_{(s,l)} - \eta(s,l)\right)\rho_a(\lambda_4) = \rho_c(\lambda_3) - \eta(s,l)\rho_c(\lambda_4)$$

This can be re-arranged for convenience as:

$$\left(\eta(s,l) - \varepsilon_{(s,l)}\right)\rho_a(\lambda_4)) = \eta(s,l)\rho_c(\lambda_4) - \rho_c(\lambda_3)$$

Finally the aerosol scattering reflectance in band 4 is obtained as,

$$\rho_a(\lambda_4) = \frac{\left[\eta(s,l)\rho_c(\lambda_4) - \rho_c(\lambda_3)\right]}{\left(\eta(s,l) - \varepsilon_{(s,l)}\right)} \tag{37}$$

Substituting for $\rho_a(\lambda_4)$ in equation (34):

$$Tv(\lambda_4)\rho_w(\lambda_4) = \rho_c(\lambda_4) - \frac{\left[\eta(s,l)\rho_c(\lambda_4) - \rho_c(\lambda_3)\right]}{\left(\eta(s,l) - \varepsilon_{(s,l)}\right)}$$

Expanding,

$$Tv(\lambda_4)\rho_w(\lambda_4) = \frac{\left(\eta_{(s,l)} - \varepsilon_{(s,l)}\right)\rho_c(\lambda_4) - \eta_{(s,l)}\rho_c(\lambda_4) + \rho_c(\lambda_3)}{\left(\eta_{(s,l)} - \varepsilon_{(s,l)}\right)} \quad (38)$$

Collecting the like terms in equation (38), the water leaving reflectance in band 4 can then be calculated as:

$$Tv(\lambda_4)\rho_w(\lambda_4)) = \left[\frac{\rho_c(\lambda_3) - \varepsilon_{(s,l)}\rho_c(\lambda_4)}{\left(\eta(s,l) - \varepsilon_{(s,l)}\right)}\right] \quad (39)$$

From equations (31) and (37), it follows therefore that aerosol scattering reflectance in band 3 can be obtained as:

$$\rho_a(\lambda_3) = \varepsilon_{(s,l)}\left[\frac{\left[\eta(s,l)\rho_c(\lambda_4) - \rho_c(\lambda_3)\right]}{\left(\eta(s,l) - \varepsilon_{(s,l)}\right)}\right] \quad (40)$$

Extending a similar approach to the other bands, the different values of aerosol scattering reflectances, $\rho_a(\lambda)$ were determined. Subtracting these from the respective Rayleigh corrected reflectances, $\rho_c(\lambda)$ for each spectral band, the water leaving reflectance, WLR in the specific band was calculated by implementing a modified version of equation (28) as:

$$\rho_w(\lambda) = \frac{\rho_c(\lambda) - \rho_a(\lambda)}{Tv(\lambda)} \quad (41)$$

The general procedure for atmospheric correction is shown in Figure 4-1.

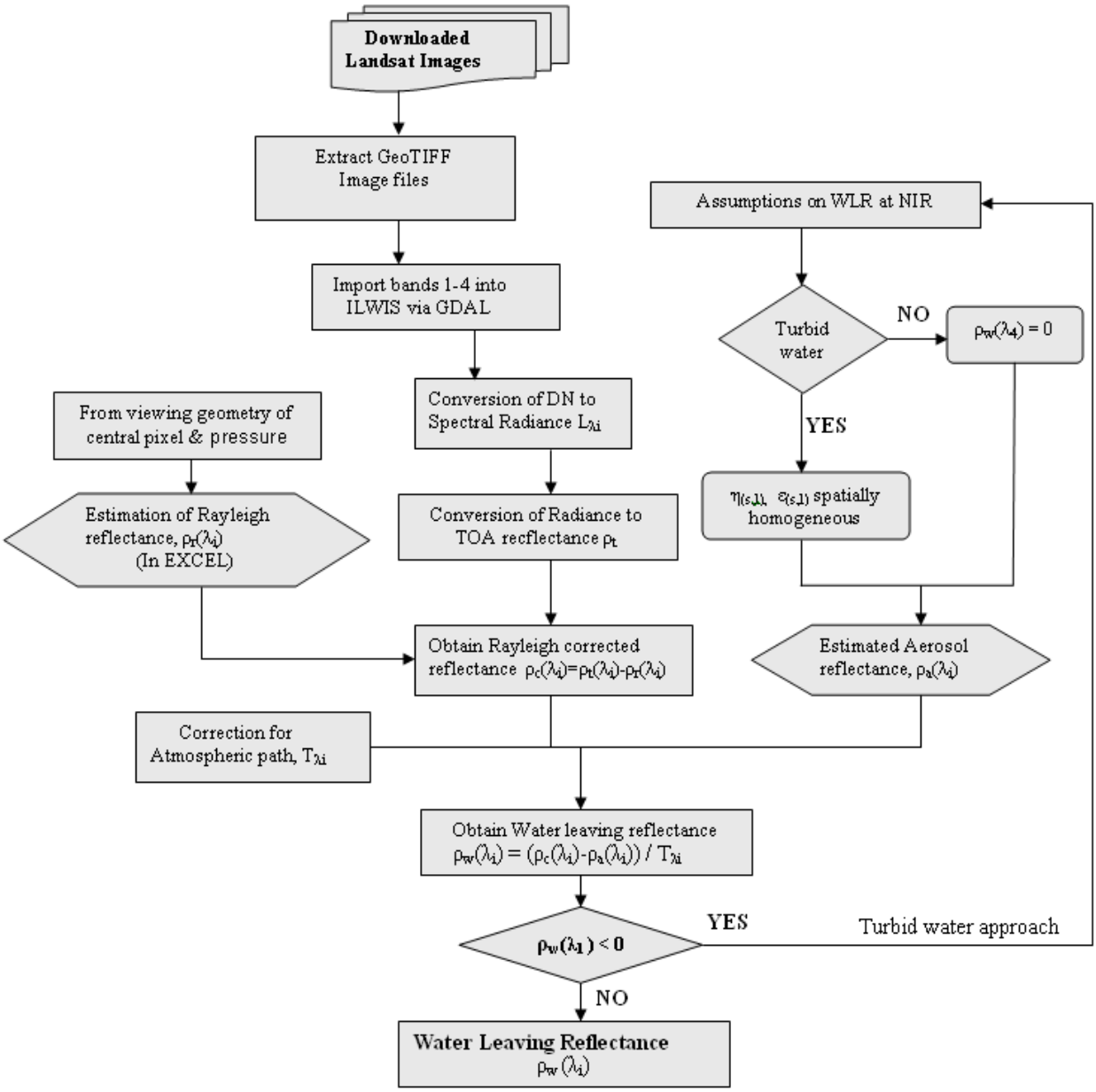

Figure 4-1: Flow chart of general procedure followed in the implementation of atmospheric correction on Landsat images

4.4. Parameterisation of IOPs and estimation of water quality variables

For inland waters, the total absorption and scattering of incident radiation can be attributed to three independently varying constituents, namely: chlorophyll-a (Chla), detritus and dissolved organic matter (dg) and suspended particulate matter (SPM).

The bulk absorption and backscattering are the sum of all absorption and backscattering of water and its constituents:

$$a(\lambda) = a_w(\lambda) + a_{ph}(\lambda) + a_{dg}(\lambda) \quad (42)$$

$$b_b(\lambda) = 0.5b_w(\lambda) + \gamma b_{spm}(\lambda) \quad (43)$$

where a_w and b_w , the absorption and scattering coefficients of water molecules are assumed constant with their values available in (Mobley, 1994; Pope and Fry, 1997) respectively.

(Maritorena et al., 2002) approximate the total absorption of phytoplankton pigments in order to parameterize Chla as:

$$a_{ph}(\lambda) = a_{ph}^*(\lambda)Chla \quad (44)$$

where a_{ph}^* is the Chla specific absorption coefficient

Owing to identical spectral signatures (Maritorena et al., 2002), the absorption attributable to detritus and dissolved organic matter can be summed and approximated as (Bricaud et al., 1981):

$$a_{dg}(\lambda) = a_{dg}(440)\exp\left[-s(\lambda - 440)\right] \quad (45)$$

where *s* is the known spectral shape exponent. Its value is taken as s=0.0206 nm^{-1} as used by (Maritorena et al., 2002) to take care of the combined effects of detritus and dissolved organic matter. From(Kopelevich, 1983), the scattering coefficient of SPM can be parameterized as:

$$b_{spm}(\lambda) = b_{spm}(550)\left(\frac{550}{\lambda}\right)^y \quad (46)$$

where *y* is the known spectral shape parameter. Its value is taken as y= 1.0337, also taken from (Maritorena et al., 2002)

The backscattering fraction γ, can be estimated from a scattering phase function (Petzold, 1977) as 0.0183.

An explicit relationship between IOPs, SIOPs, water constituent concentrations and WLR can be obtained following the Lambert-Beer law. This relationship is expressed as a linear system of equations following (Hakvoort et al., 2002) as : $A\mathbf{x} = y$, with:

$$A = \rho_w(\lambda)a_{ph}^*{}_{\lambda=1\ldots n}, \rho_w(\lambda)a_{dg}^* cdom_{\lambda=1\ldots n}, \rho_w(\lambda)b_{spm}^* \quad (47)$$

$$y = \left(-\rho_w(\lambda)\left[a_w + b_w\right] + b_{w\,\lambda=1..n}\right) \quad (48)$$

and

$$\mathbf{x} = \begin{bmatrix} CHL \\ CDOM \\ SPM \end{bmatrix} \tag{49}$$

where ($a_{dg}^*(\lambda)$, $b_{spm}^*(\lambda)$) are the specific absorption coefficient of CDOM and specific backscattering coefficient of SPM.

Following Cramer's rule, the concentrations of the water quality variables can be obtained after an inversion of the updated semi-analytical bio-optical model in vector form from the visible spectral range as shown in equation (49)

4.5. Empirical determination of water quality variables

Following a poor performance of the proposed semi-analytical model, an empirical physical model was used to estimate water quality variables from WLR.

The Area Chlorophyll-a Concentration Retrieval Model (ACCRM) which exploits the spectral geometric triangle properties of water leaving reflectance derived from Landsat satellite data (Figure 2-1) was used to retrieve the Chla concentration.

Assuming the lines AB, BC and AC in Figure 2-1 can be denoted in vector form as follows:

$$\overrightarrow{AB} = \{Band\,2 - Band\,1, \rho_w(\lambda_2) - \rho_w(\lambda_1)\} \tag{50}$$

$$\overrightarrow{AC} = \{Band\,3 - Band\,1, \rho_w(\lambda_3) - \rho_w(\lambda_1)\} \tag{51}$$

$$\overrightarrow{BC} = \{Band\,3 - Band\,2, \rho_w(\lambda_3) - \rho_w(\lambda_2)\} \tag{52}$$

The area of triangle ABC, S, was calculated as:

$$S = \frac{\left|\overrightarrow{AB} \times \overrightarrow{AC}\right|}{2} = \frac{0.175\rho_w(\lambda_2) - \left(0.1\rho_w(\lambda_1) + 0.075\rho_w(\lambda_3)\right)}{2} \tag{53}$$

Following ACCRM, Chla concentration was exponentially related to the area of the triangle from which Chla concentration in μgl^{-1} was then determined as:

$$Chla = F\exp(102.68S) \tag{54}$$

where F is a unitless fitting factor and was determined empirically for the Poyang Lake as 0.270706 while the value 102.68 is a coefficient taken from the exponential trend line equation relating Chla to area of triangle.

SPM in mgl^{-1} was then determined from the estimated Chla concentration as:

$$SPM = \frac{a_{ph}{}^*{}_{\lambda=1\ldots n}\, Chla + a_{ph}{}^*{}_{\lambda=1\ldots n} + Chla(\lambda_2)}{\left(f/\rho_w(\lambda_1) - 1\right)} \tag{55}$$

where f=16.1%; an empirical factor.

5. Results and Discussions

Water leaving reflectances were obtained following an implementation of the image-based case 2 water atmospheric correction algorithm described earlier.

An attempt to derive IOPs using an updated semi-analytical model obtained following the adaptation of the Gordon reflectance bio-optical model for Landsat imagery was unsuccessful. The implementation of the proposed algorithm yielded physically unrealistic results. The concentrations of Chlorophyll-a were negative while those of SPM were extremely large and in the range of over 700 mgl^{-1} . Nonetheless, following an empirical approach, a linear model that exponentially related Chla concentration to water leaving reflectance was used to estimate Chla and SPM concentrations from the three Landsat bands.

Owing to a lack of in-situ measurements for dissolved organic matter, no analysis on the same is undertaken.

With in-situ measurements of both WLR and concentrations of Chla and SPM taken in 30 sites over 3 different days, only 15 field measurement sites were corresponding to the Landsat satellite imagery acquired over the Poyang Lake on October 15th, 2008. The valid retrievals lay over 9 sites for same day imagery and field measurements and 20 sites for entire duration of field measurements. This results in an even smaller data set upon which the statistical analyses of the performance of the algorithms were undertaken.

For validation, the statistical parameters of model II regression (Laws, 1997) were used to evaluate the match between satellite derived and known values from in-situ measurements on the Poyang Lake. The assessment of the absolute errors in the methods applied was also obtained by computing the root mean square errors (RMSE). RMSE is the standard deviation of the differences between the satellite derived values and in-situ measurements. The RMSE was computed as:

$$RMSE = \left(\frac{1}{N} \sum_{i=1}^{N} \left[\log\left(P_i^{derived} \right) - \log\left(P_i^{measured} \right) \right]^2 \right)^{0.5} \quad (56)$$

where $P_i^{derived}$ stands for the i^{th} property derived from satellite imagery, $P_i^{measured}$ for the i^{th} property known from in-situ measurements and N is the number of valid retrievals.

5.1. Satellite derived and in-situ measured water leaving reflectance

An implementation of the image based atmospheric correction algorithm described earlier on the satellite imagery yielded water leaving reflectances in bands 1-3 of Landsat. Satellite derived and in-situ measured WLR obtained on the same day are compared in a scatter plot to show the overall accuracy of the model used (Figure 5-1). In general, the results show that the satellite derived values

are close to the measured values and present a good fit with a linear correlation coefficient square (R^2) of 0.797 and RMSE of 0.117.

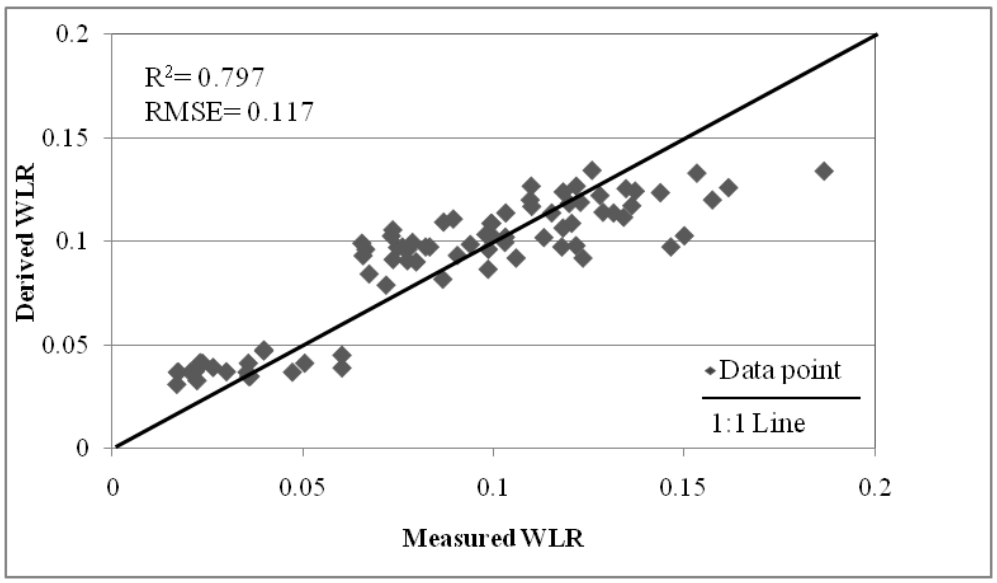

Figure 5-1: Comparison between the derived and measured water leaving reflectances with match up sites of the Poyang Lake

An analysis of the satellite derived and in-situ measured water leaving reflectances in the individual bands gives band specific results which are presented in a scatter plot shown in Figure 5-2.

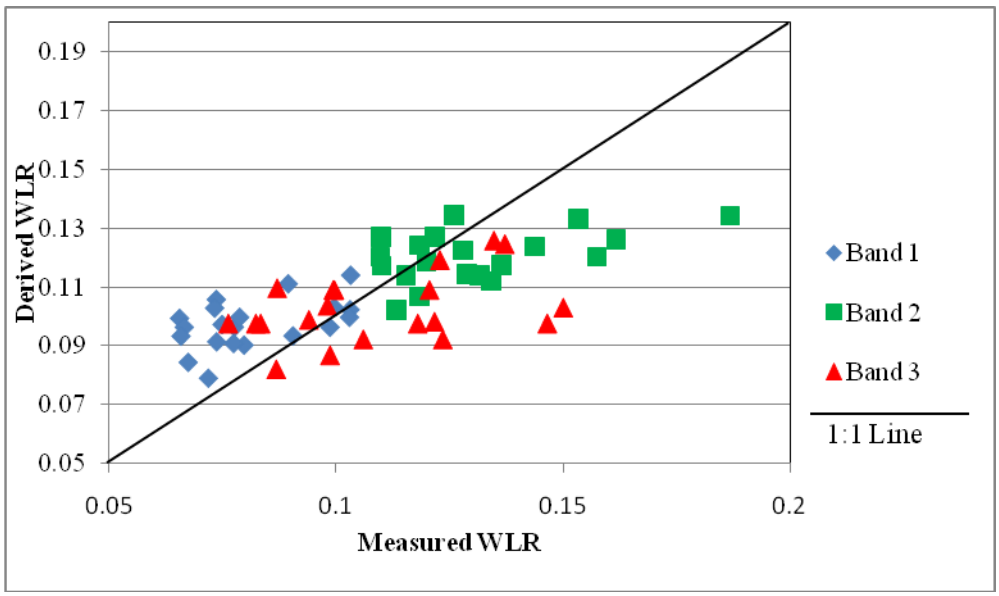

Figure 5-2: Comparison between the derived and measured water leaving reflectances with match-up sites of the Poyang Lake for Bands 1-3

The plot still shows a generally good fit between the satellite derived and in-situ measured water leaving reflectance. The statistical parameters of model II regression and the computed RMSE for the specific bands are presented in Table 5-1 for measurements taken on the same day the satellite image was acquired and Table 5-2 for the entire dataset.

Table 5-1: RMSE and type II regression parameters between satellite derived and field measured water leaving reflectances with both field measurements and satellite image acquired on the same day

Parameter	Nr. Samples	Slope	Intercept	R^2	RMSE
Band 1	9	0.3062	0.0734	0.3344	0.0982
Band 2	9	0.2523	0.0869	0.4405	0.0792
Band 3	9	0.2124	0.0788	0.1546	0.0981

Table 5-2: RMSE and type II regression parameters between satellite derived and field measured water leaving reflectances with measurements obtained over a 3 day period

Parameter	Nr. Samples	Slope	Intercept	R^2	RMSE
Band 1	20	0.3038	0.0726	0.2467	0.0998
Band 2	20	0.2032	0.0938	0.2271	0.0643
Band 3	20	0.2069	0.08	0.1602	0.0829

A comparison between the RMSE reflectances obtained from same day data match-ups and the entire data set shows only a slight variation (Figure 5-3) in the values. This indicates that satellite derived reflectances in bands 1-3 are fairly accurately estimated despite the different dates the in-situ measurements were obtained.

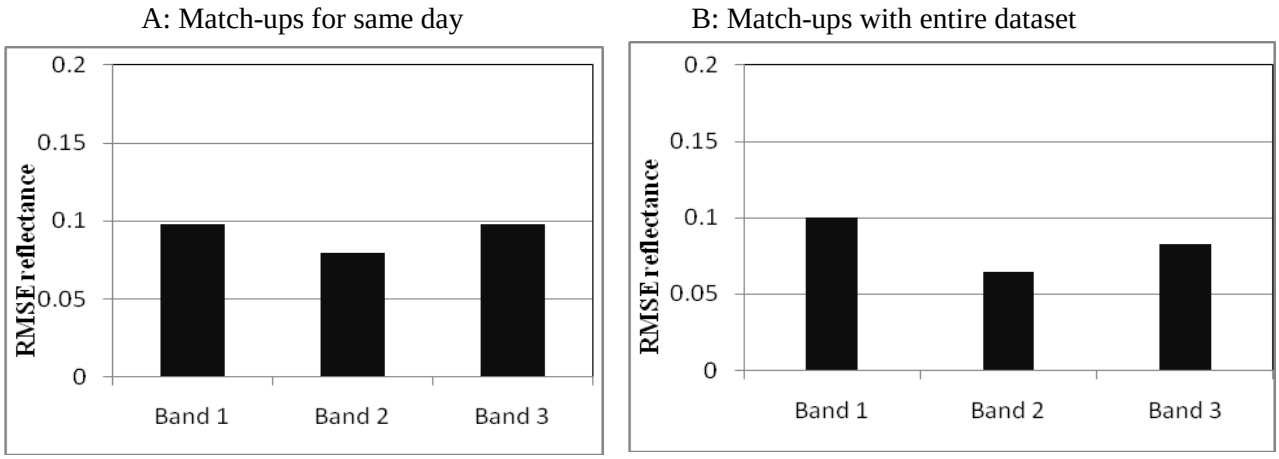

Figure 5-3: The root mean square errors between satellite derived and field measured water leaving reflectances in bands 1-3: A; measurements on same day as image acquisition and B; measurements taken over 3 days

5.1.1. Limitations in estimation of water leaving reflectances from Landsat imagery

A number of assumptions and approximations were made in the atmospheric correction algorithms applied in this study and can be found in the methodology.

However, the most important assumptions made were that the ratios of Aerosol reflectances and WLR in the NIR bands were spatially homogeneous and taken as constant. Taking Landsat bands 3 and 4 in these ratios has an inherent limitation, due to the fact that band 3 lies in the visible spectral range. This is due to the broad spectral bands of the Landsat sensor.

The assumption of spatial homogeneity in the ratio of Aerosol reflectances in the NIR bands, $\varepsilon_{(s,l)} = \rho_a(\lambda_3) / \rho_a(\lambda_4)$ is based on the fact that though aerosol concentrations can vary considerably over small space scales, the aerosol type is expected to vary only weakly in space (Ruddick et al., 2000). The shortcomings of this assumption notwithstanding, it holds true for small spatial scales.

The WLR are retrieved following two different approaches for correction of atmospheric effects. The standard approach in which WLR in the NIR band (band 4) was assumed to be zero and the turbid water atmospheric correction which was applied on one image after the implementation of the standard approach yielded negative WLR in shorter wavelength bands in this image. This was due to the fact that in turbid waters it is no longer true that WLR in the NIR band is zero.

The WLR ratio $\eta(s,l) = \rho_w(\lambda_3) / \rho_w(\lambda_4)$, was determined as 2.55. This value was arrived at by fitting the relation between in-situ measurements of WLR and the satellite derived Rayleigh corrected reflectances from the Poyang Lake using the equation:

$$\eta(s,l) = \varepsilon_{(s,l)}\rho_m(\lambda_3)\left[\rho_m(\lambda_3) - \left(\frac{\rho_c(\lambda_3) - \varepsilon_{(s,l)}\rho_c(\lambda_4)}{Tv(\lambda_3)}\right)\right]^{-1} \quad (57)$$

where ρ_m is the in-situ measured WLR.

Applying this value on the Roxo reservoir would lead to inherent errors since it has not been locally fitted. Further, the WLR in the NIR in turbid waters can no longer be considered constant and varies with turbidity as shown by (Salama et al., 2009b). The WLR ratio $\eta(s,l)$ will thus vary spatially in turbid waters resulting in more errors in the estimation of WLR when it is assumed homogeneous and constant.

Figure 5-4 shows the satellite derived WLR maps of the Roxo reservoir. The standard approach to atmospheric correction was applied on the images acquired on September 5th, 2000 and July 4th, 2002 while the turbid water atmospheric correction was applied on the image acquired on June 4th, 2001.

5.2. Satellite estimated water quality variables

5.2.1. Estimation of water quality variables by inversion of modified bio-optical model

An inversion of the updated Gordon reflectance semi-analytical bio-optical model to estimate water quality variables from Landsat on Roxo reservoir was unsuccessful. This can be attributed to three main reasons: an over correction for atmospheric effects, the limitations imposed on the model due to the parameterisation of IOPs and the instability of the numerical matrix inversion.

The WLR ratio $\eta(s,l)$ is expected to be a smooth function of SPM (Carder et al., 1999; Ruddick et al., 2000) and was therefore assumed constant. However as shown earlier, this argument does not hold for optically complex inland waters. Fitting $\eta(s,l)$, a constant in equation (40) and applying it on Roxo reservoir would result in an error of ±15% due to an over correction of atmospheric effects due to aerosols. $\eta(s,l)$ was therefore varied to fit the model to compensate for the low spectral sensitivity and broad bands of Landsat.

(Salama et al., 2009a) argue that the parameterisations for the IOPs in equations (44), (45) and (46) are inadequate for inland waters with extreme absorption and scattering values. This is because each parameterisation poses unique limitations on the model. Different species of phytoplankton may co-exist in inland water leading to great variability in Chla absorption in nature (Bricaud et al., 1998; Carder et al., 1999). This is not considered in equation (44). By attributing absorption due to detritus and DOM in one spectral shape and parameter, equation (45) imposes a constant slope, *S* for the spectral decrease in a_{dg} absorption which is not the case in nature. This has been shown to depend on a number of factors including interactions between water and land, productivity and state of phytoplankton colonies and photochemistry (Maritorena et al., 2002). Similarly, holding the spectral shape parameter, *y* in equation (46) constant to model particulate backscattering is inaccurate since the wavelength dependence assumed has been known to disappear in optically complex waters (IOCCG, 2006).

Also, the IOPs and SIOPs used in the relations to estimate water quality variables were all taken from literature and were measured in water bodies other than Roxo reservoir. This in itself degrades the ability of the model to retrieve water quality parameters from satellite imagery for the intended study area.

The instability of the numerical inversion of the semi-analytical bio-optical model was due to the fact that very few bands were used as inputs into the model (few samples) and yet a number of errors were generated during image processing. With only 3 bands centered at 483nm, 560nm and 662 nm in the case of Landsat ETM as input bands in the bio-optical model, the inversion failed to gain stability owing to a propagation of rounding errors with large residuals.

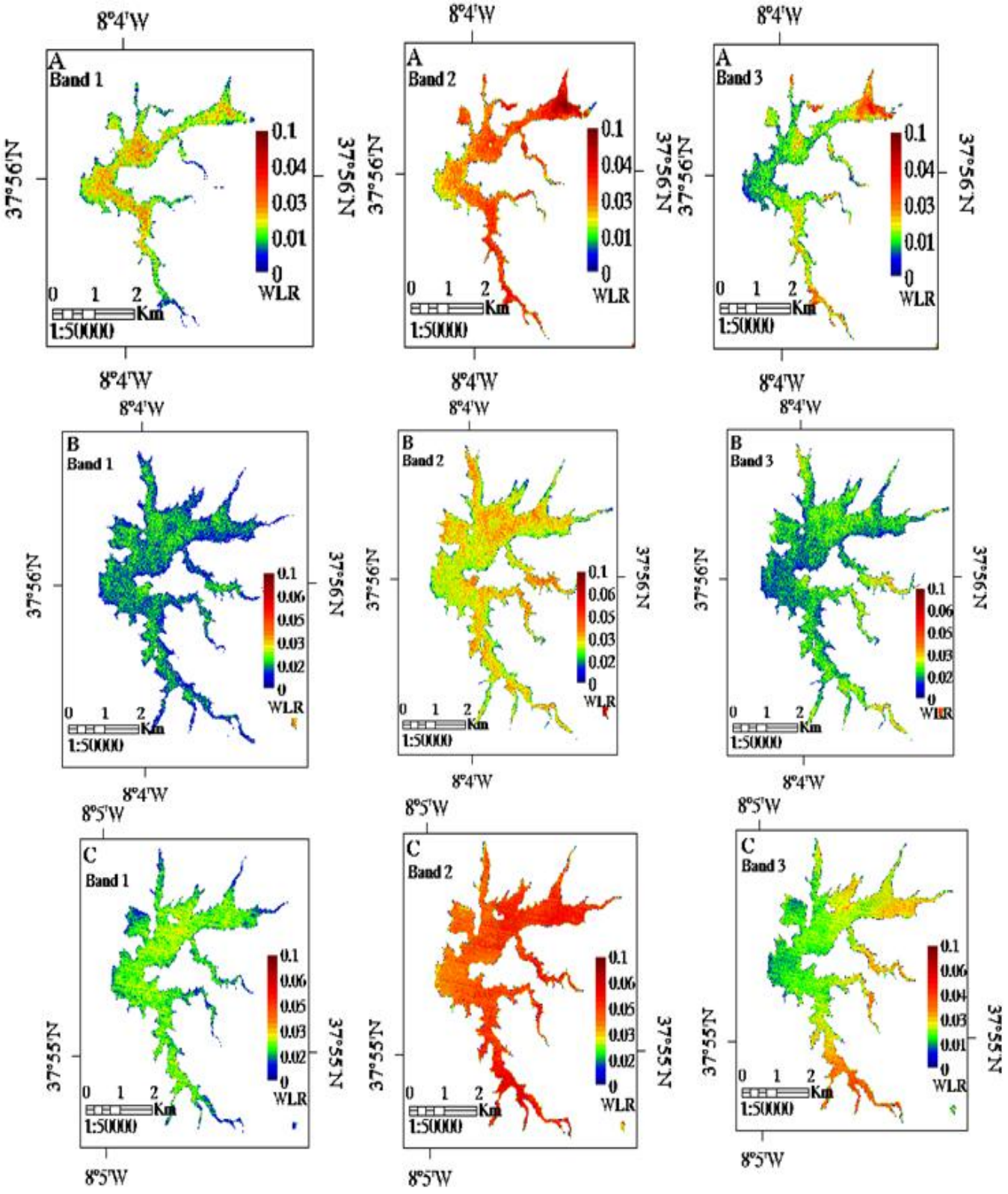

Figure 5-4: Water leaving reflectance maps of Roxo reservoir obtained after atmospheric correction of Landsat images acquired on (A) 05-09-2000 (B) 04-06-2001 and (C) 01-07-2002

5.2.2. Estimation of water quality variables using the ACCRM model

With the poor performance of the bio-optical model, an empirical component used to derive Chla and SPM concentrations was incorporated in the model. The empirical approach was able to quantify Chla and SPM concentration by using the WLR in the 3 Landsat bands as inputs.

The outputs of the ACCRM model of Chla and SPM were validated using the Poyang Lake in-situ data set. Two sets of analyses were undertaken in the validation. The first is based on analysis of products with in-situ measurements acquired on the same day as the satellite image denoted by suffix 9 representing number of valid match-ups and the second with all the in-situ measurements which were obtained over 3 days denoted by suffix 20.

Chla concentrations derived were in the range 0.31 μgl^{-1} to 0.35 μgl^{-1}. The R^2 values for Chla increased from 0.192 to 0.295 when the statistical analysis was performed using all measurements (Figure 5-5) and then with only match-ups for measurements acquired on the same day as the satellite image (Figure 5-6)

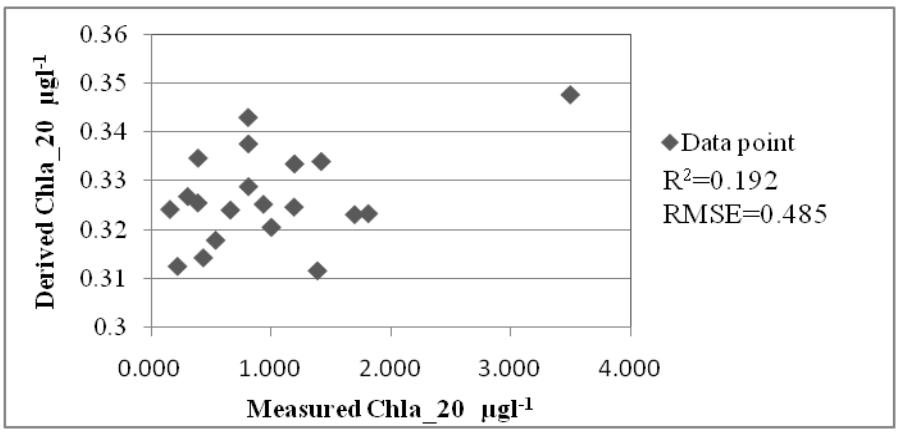

Figure 5-5: Comparison of the empirically derived and measured concentrations of Chlorophyll-a with match-up sites of the Poyang Lake with field measurements obtained over a 3 day period

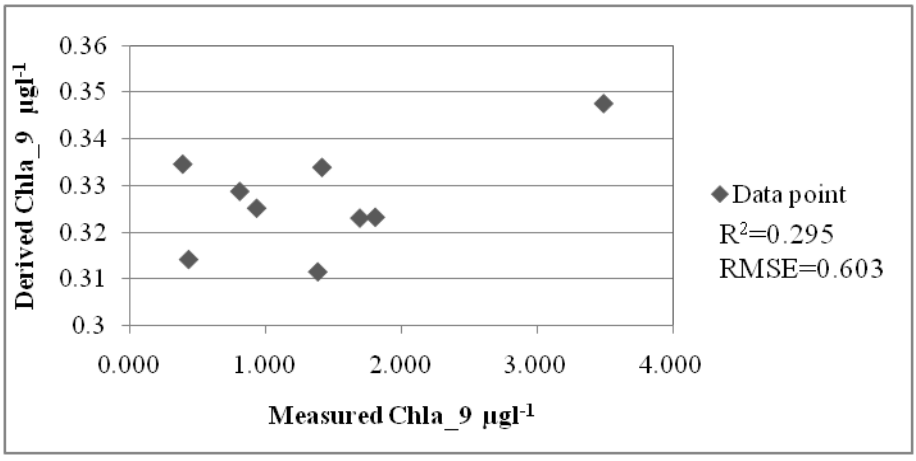

Figure 5-6: Comparison between the empirically derived and measured concentrations of Chlorophyll-a with match-up sites of the Poyang Lake with both field measurements and satellite image acquired on the same day

A summary of the RMSE values and type II regression statistics for Chla concentrations retrieved are presented in Table 5-3

Table 5-3: RMSE and type II regression parameters between satellite derived and field measured concentrations of Chlorophyll-a with match-up sites of the Poyang Lake with field measurements obtained on the same day as satellite image(Chla_9) and over a 3 day period

Parameter	Nr. Samples	Slope	Intercept	R^2	RMSE
Chla_9	9	0.0063	0.3184	0.295	0.603
Chla_20	20	0.0055	0.3213	0.192	0.485

Though Chla concentration retrievals are closer to the measured values when same day match ups are considered, the R^2 value is still considerably low. This is due to the fact that Landsat has a low spectral resolution and is less sensitive to Chla owing to its broad spectral bands. In addition to Chla, the water column contains a mixture of dissolved organic matter and inorganic suspended sediment. These substances have brighter spectral signatures than Chla (Giardino et al., 2001) and would therefore overshadow the spectral signature of Chla in a low spectral resolution sensor such as Landsat. Figure 5-7 shows that there is no discernible relation or trend between Chla concentration and the derived WLR reflectances in bands 1, 2 and 3 of Landsat.

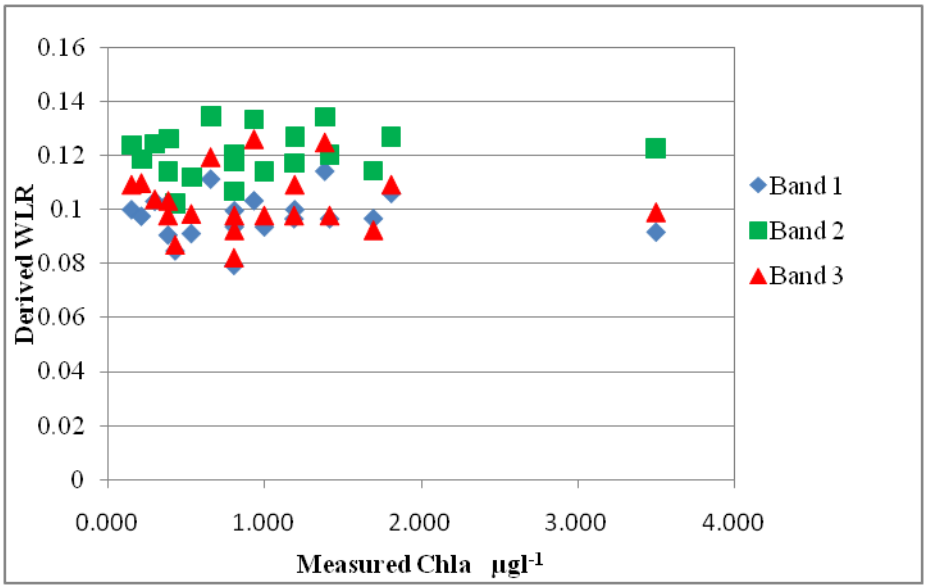

Figure 5-7: Scatter plot showing relationship between measured concentrations of Chla and the derived WLR in the different bands

The absorption maxima of Chla in the absorption spectra lie at 440 nm and 662 nm wavelengths. As seen in Figure 5-8, Landsat spectral range does not cover the absorption maxima at 440nm since Landsat band 1 is from 452nm to 512nm with the central wavelength at 483nm(ETM). (Salama et al., 2009a) reveal that this absorption feature is critical for reliable Chla retrievals and its exclusion

therefore, compromises Chla estimation from Landsat. This shows that Landsat sensors are not suitable for Chla measurements.

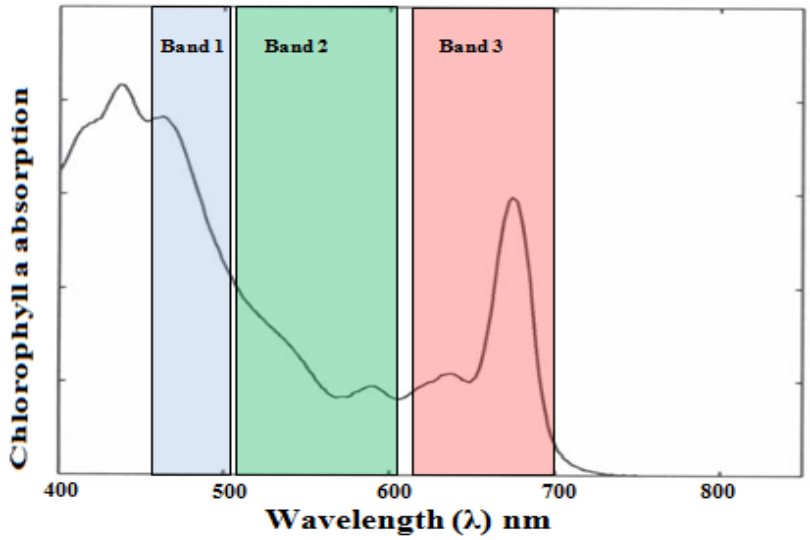

Figure 5-8: Chlorophyll a absorption spectra and Landsat spectral bands 1, 2 and 3

For SPM, the derived concentrations were between 9 mgl^{-1} to 34 mgl^{-1} for the Poyang Lake. When all measurements were used in the statistical analysis during the validation of the retrievals, the R^2 value was 0.28 for a linear fit (Figure 5-9). This value rose to 0.5 when only the measurements obtained on the same day as image were considered (Figure 5-10). This shows a relatively high correlation between the derived and measured concentrations of SPM.

It is critical however, to point out that SPM was derived based on its relationship with Chla and as such can only be as reliable as the Chla retrievals. A further analysis of the variation in SPM concentration with time by fitting the most appropriate trend line shows that a 4^{th} order polynomial fit best describes the sinusoidal decomposition of SPM with time with a correlation coefficient R^2 of 0.64 and is shown in Figure 5-11.

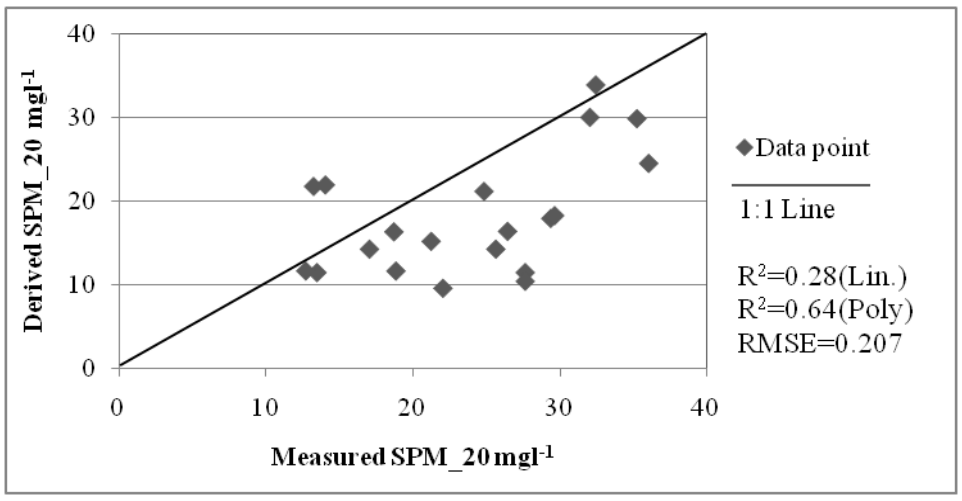

Figure 5-9: Comparison of the empirically derived and measured concentrations of SPM with match-up sites of the Poyang Lake with field measurements obtained over a 3 day period

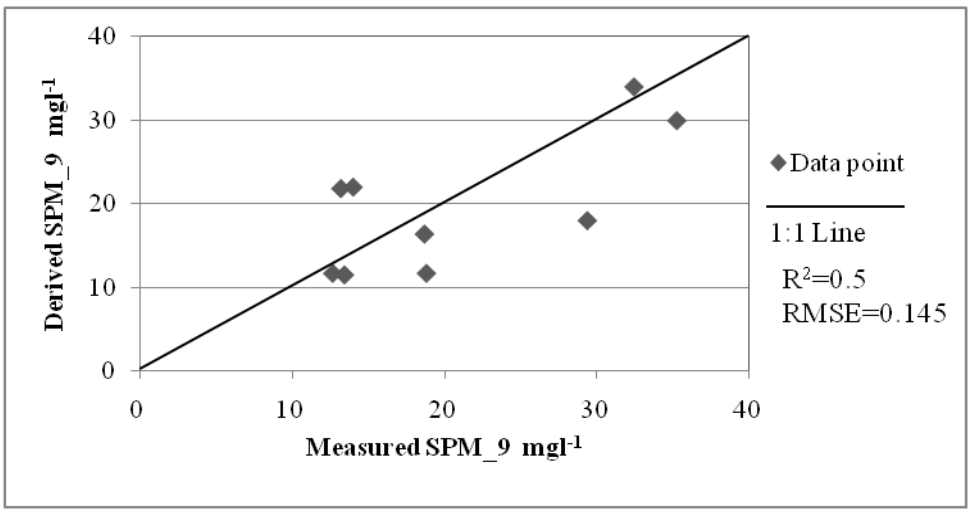

Figure 5-10: Comparison between the empirically derived and measured concentrations of SPM with match-up sites of the Poyang Lake with both field measurements and satellite image acquired on the same day

A summary of the RMSE values and type II regression statistics for SPM concentrations retrieved over the Poyang Lake are presented in Table 5-4

Table 5-4: RMSE and type II regression parameters between satellite derived and field measured concentrations of SPM with match-up sites of the Poyang Lake with field measurements obtained on the same day as satellite image (SPM_9) and over a 3 day period (SPM_20)

Parameter	Nr. Samples	Slope	Intercept	RMSE	R^2
SPM_9	9	0.64	6.24	0.145	0.5
SPM_20	20	0.50	6.09	0.207	0.28 (linear fit)
					0.64 (4^{th} order polynomial fit)

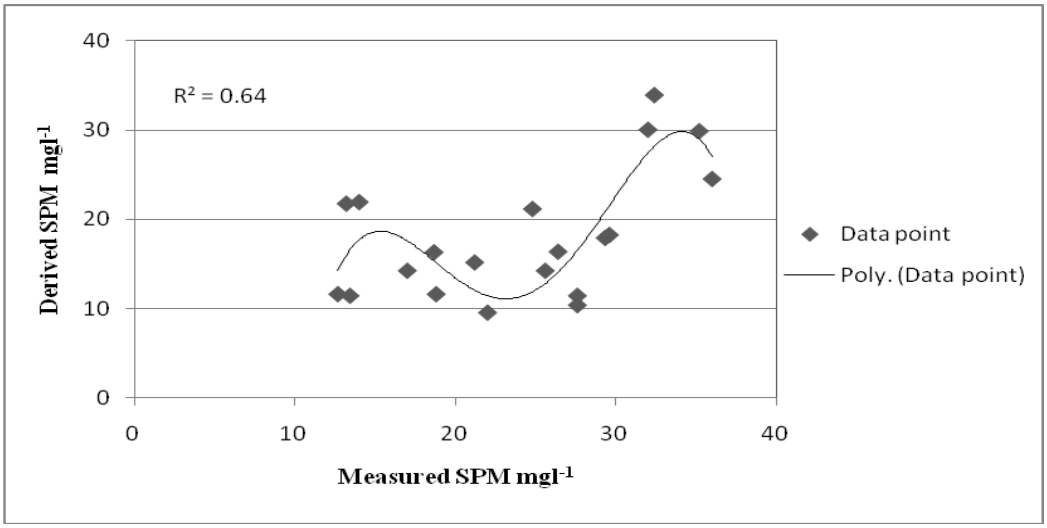

Figure 5-11: The variation between satellite derived and measured concentrations of SPM over a 3 day period

The derived Chla and SPM maps for Roxo reservoir are shown in Figure 5-12

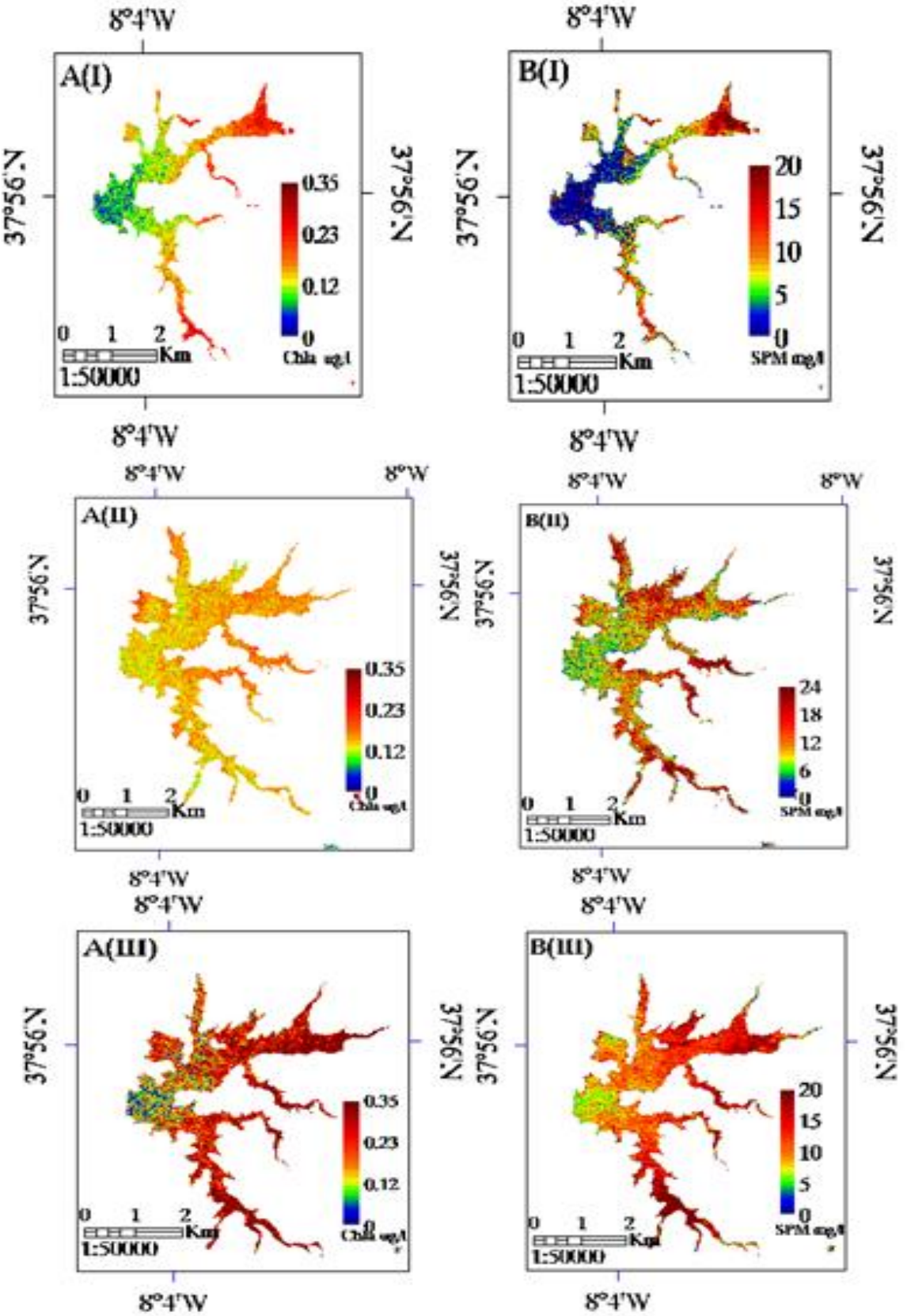

Figure 5-12: Derived (A) Chla and (B) SPM concentration maps of the Roxo reservoir estimated from Landsat images acquired on (I) 05-09- 2000; (II) 04-06-2001 and (III) 01-07-2002 using the ACCRM model

6. Conclusions and Recommendations

6.1. Conclusions

6.1.1. Image based atmospheric correction

Two image based models have been used to estimate water leaving reflectance from Landsat images in this study. The first is an adaptation for Landsat of the standard SeaWiFS atmospheric correction algorithm while the second was an adaptation of the same algorithm to achieve atmospheric correction over turbid waters. The difference between the two is due to the fact that water leaving reflectance in the NIR may be significant over turbid water and yet the standard model assumes it is negligible.

The turbid water atmospheric correction model was implemented only on images for which the standard approach failed. The standard approach fails because non-zero water-leaving signal in turbid waters in the NIR result in an over estimation of the aerosol scattering reflectance and therefore, an atmospheric "over-correction" in the visible part of the spectrum.

The model results of water leaving reflectance estimation from Landsat show a good correlation (R^2=0.797) with field measurements on the Poyang Lake. However, this correlation reduces dramatically when analyses were carried out on the individual bands. This can be attributed to the spectral and spatial variability of atmospheric components which were aggregated leading to an inadequate characterisation of atmospheric effects in the models, in addition to the low spectral sensitivity of Landsat as a result of its broad bands. The use of Landsat bands 3 and 4 in the formulations for aerosol reflectance and WLR ratios is bound to be inadequate since band 3 is clearly in the visible spectral range.

6.1.2. Inversion of bio-optical model for local situation

The updated semi-analytical bio-optical model was not sufficient for retrieval of water quality variables using Landsat imagery. The failure of the model can be attributed to the inherent limitations in Landsat imagery for water characterisation since it was intended for use with high spectral and low spatial resolution satellite data for which the converse is true for Landsat.

A number of model inputs were held constant and yet they are known to vary in nature (IOCCG, 2006). The IOPs and SIOPs used in parameterisations were tuned using a global dataset. To be applied on Roxo reservoir would require local measurements of the same.

6.1.3. Empirical estimation of Chla and SPM

The concentrations of Chla and SPM were obtained using an empirical method that required only water leaving reflectance in the 3 visible bands. The ACCRM model used in the estimation of these water quality parameters was able to derive Chla and SPM concentrations, with R^2 values of 0.295 and

0.5 respectively, for in-situ measurements taken on same day image was acquired. The results agree with the limitations of Landsat to accurately retrieve Chla.

Though SPM measurements return better statistics, it is critical to know they are directly inferred from Chla.

The numerous challenges involved in comparing earth observation data with in-situ measurements notwithstanding, the results of this exploratory study show that remote sensing can be a versatile tool in water quality estimation for monitoring purposes.

6.1.4. Water quality estimation using the Landsat sensor

This study has shown that Landsat is not well suited for determination of Chla due to its low spectral sensitivity as well as broad bands. The sensor is not able to capture any information below 450nm which is the lower end of Landsat band 1 and yet there is a critical Chla absorption peak at 440nm.

The low spectral and temporal resolutions of Landsat limit its ability in rapid water quality monitoring programmes. Nonetheless, the high spatial resolution makes it suitable for water quality studies in small inland lakes and other water bodies.

In conclusion, despite the fact that Landsat sensors were principally designed for mapping land surfaces and are therefore limited in their ability to accurately characterise water surfaces, several studies have proved they can be useful in inland water studies. With the Landsat Data Continuity Mission yet to be launched, it is evident that Landsat will continue to play a dominant role in earth observation science for the foreseeable future. It is therefore imperative that models that use Landsat data for inland water quality applications be developed.

6.2. Recommendations

The performance of the atmospheric correction models used in this study are heavily dependent on the accurate characterisation of the aerosol reflectance components. These models can therefore be improved by taking into consideration the impact of aerosol scattering on atmospheric transmittance, multiple scattering effects, as well as light absorption by atmospheric gasses such as water vapour and carbon dioxide.

With the realisation of more reliable atmospheric correction models, it is envisaged that even the outputs of the semi-analytical bio-optical model can be improved.

There is a need also, to tune the model before it is used in any specific area. This requires an extensive data set of radiometric (WLR) and water quality (Chla and SPM) in-situ measurements from the area.

The biggest challenge in this study was the lack of in-situ WLR and Chla and SPM measurements on the Roxo reservoir. Independent calibrations of the models as well as validation of atmospheric correction outputs and remotely sensed products were not possible. I therefore recommend an

intensive field campaign be carried out on the Roxo reservoir with the aim of acquiring these measurements.

REFERENCES

Baban, S.M.J., 1993. Detecting Water-quality Parameters in the Norfolk Broads, UK, using Landsat Imagery. International Journal of Remote Sensing, 14(7): 1247-1267.

Bricaud, A., Morel, A., Babin, M., Allali, K. and Claustre, H., 1998. Variations of light absorption by suspended particles with chlorophyll a concentration in oceanic (case 1) waters: Analysis and implications for bio-optical models. Journal of Geophysical Research-Oceans, 103(C13): 31033-31044.

Bricaud, A., Morel, A. and Prieur, L., 1981. Absorption by dissolved organic matter of the sea (yellow substance) in the UV and visible domains. Limnology and Oceanography, 26(1): 11.

Brivio, P.A., Giardino, C. and Zilioli, E., 2001. Validation of satellite data for quality assurance in lake monitoring applications. The Science of The Total Environment, 268(1-3): 3-18.

Carder, K.L., Chen, F.R., Lee, Z.P., Hawes, S.K. and Kamykowski, D., 1999. Semianalytic Moderate-Resolution Imaging Spectrometer algorithms for chlorophyll a and absorption with bio-optical domains based on nitrate-depletion temperatures. Journal of Geophysical Research-Oceans, 104(C3): 5403-5421.

Carpenter, D.J. and Carpenter, S.M., 1983. Modeling inland water quality using Landsat data. Remote Sensing of Environment, 13(4): 345-352.

Chander, G., Markham, B.L. and Helder, D.L., 2009. Summary of current radiometric calibration coefficients for Landsat MSS, TM, ETM+, and EO-1 ALI sensors. Remote Sensing of Environment, 113(5): 893-903.

Chen, J., Zhou, G., Wen, Z. and Xiao, Z., 2009. Spectral Geometric Triangle Properties of Chlorophyll-a Inversion in Turbid Waters based on TM Data: A Case Study of Taihu Lake. Canadian Journal of Remote Sensing.

Chomko, R.M., Gordon, H.R., Maritorena, S. and Siegel, D.A., 2003. Simultaneous retrieval of oceanic and atmospheric parameters for ocean color imagery by spectral optimization: a validation. Remote Sensing of Environment, 84(2): 208-220.

Dekker, A.G. and Peters, S.W.M., 1993. The use of the Thematic Mapper for the analysis of Eutrophic Lakes- A case study in the Netherlands. International Journal of Remote Sensing, 14(5): 799-821.

Dekker, A.G., Vos, R.J. and Peters, S.W.M., 2001. Comparison of remote sensing data, model results and in situ data for total suspended matter (TSM) in the southern Frisian lakes. Science of The Total Environment, 268(1-3): 197-214.

Dekker, A.G., Vos, R.J. and Peters, S.W.M., 2002. Analytical algorithms for lake water TSM estimation for retrospective analyses of TM and SPOT sensor data. International Journal of Remote Sensing, 23(1): 15-35.

Fargion, S. and Muller, J., 2000. OCEAN Optics Protocol for Satellite Ocean Color Validation, Revision 2. Protocol. NASA.

Giardino, C., Pepe, M., Brivio, P.A., Ghezzi, P. and Zilioli, E., 2001. Detecting chlorophyll, Secchi disk depth and surface temperature in a sub-alpine lake using Landsat imagery. Science of The Total Environment, 268(1-3): 19-29.

Gordon, H., Brown, O. and Jacobs, M., 1975. Computed relationships between inherent and apparent optical-properties of a flat homogeneous ocean. Applied Optics, 14(2): 417-427.

Gordon, H. and Castano, D., 1987. Coastal color scanner atmospheric correction algorithm: multiple scattering effects. Applied Optics, 26(1): 2111-2122.

Gordon, H.R., 1997. Atmospheric correction of ocean color imagery in the Earth Observing System era. Journal of Geophysical Research-Atmospheres, 102(D14): 17081-17106.

Gordon, H.R., Brown, O.B., Evans, R.H., Brown, J.W., Smith, R.C., Baker, K.S. and Clark, D.K., 1988. A Semi analytic Radiance Model of Ocean Color. Journal of Geophysical Research-Atmospheres, 93(D9): 10909-10924.

Hakvoort, H., de Haan, J., Jordans, R., Vos, R., Peters, S. and Rijkeboer, M., 2002. Towards airborne remote sensing of water quality in The Netherlands--validation and error analysis. ISPRS Journal of Photogrammetry and Remote Sensing, 57(3): 171-183.

Hansen, J.E. and Travis, L.D., 1974. Light scattering in planetary atmospheres. Space Science Reviews, 16: 527-610.

Harrington Jr, J.A., Schiebe, F.R. and Nix, J.F., 1992. Remote sensing of Lake Chicot, Arkansas: Monitoring suspended sediments, turbidity, and Secchi depth with Landsat MSS data. Remote Sensing of Environment, 39(1): 15-27.

IOCCG, 2006. Remote Sensing of Inherent Optical Properties: Fundamentals, Tests of Algorithms, and Applications. Lee, Z.-P (ed.), Reports of the International Ocean-Colour Coordinating Group, No.5

IOCCG, Darmouth, Canada.

Jacquet, J.M. and Zand, B., 1989. Colour analysis of inland waters using Landsat TM data. Monitoring the Earth's Environment ESA SP-1102: 11.

Kishino, M., Tanaka, A. and Ishizaka, J., 2005. Retrieval of Chlorophyll a, suspended solids, and colored dissolved organic matter in Tokyo Bay using ASTER data, Remote Sensing of Environment, pp. 66-74.

Kloiber, S.M., Brezonik, P.L., Olmanson, L.G. and Bauer, M.E., 2002. A procedure for regional lake water clarity assessment using Landsat multispectral data. Remote Sensing of Environment, 82(1): 38-47.

Kopelevich, O., 1983. Small parameter model of optical properties of sea waters Physical Ocean Optics, 1.

Lathrop, R.G., 1992. Landsat Thematic Mapper Monitoring of Turbid Inland Water Quality. Photogrammetric Engineering and Remote Sensing, 58(4): 465-470.

Lathrop, R.G. and Lillesand, T.M., 1986. Use of Thematic Mapper data to assess water quality in Green Bay and Central Lake Michigan. Photo Eng Remote Sensing, 52: 10.

Lavery, P., Pattiaratchi, C., Wyllie, A. and Hick, P., 1993. Water quality monitoring in estuarine waters using the landsat thematic mapper. Remote Sensing of Environment, 46(3): 268-280.

Laws, E., 1997. Mathematical Methods for Oceanographers: An Introduction. John Wiley and Sons, New York, 343 pp.

Lee, Z.P., Carder, K.L., Mobley, C.D., Steward, R.G. and Patch, J.S., 1999. Hyperspectral remote sensing for shallow waters: 2. Deriving bottom depths and water properties by optimization. Applied Optics, 38(18): 3831-3843.

Maritorena, S., Siegel, D.A. and Peterson, A.R., 2002. Optimization of a semi analytical ocean color model for global-scale applications. Applied Optics, 41(15): 2705-2714.

Mayo, M., Gitelson, A., Yacobi, Y.Z. and Ben-Avraham, Z., 1995. Chlorophyll distribution in Lake Kinneret determined from Landsat Thematic Mapper data. International Journal of Remote Sensing, 16: 175-182.

Mobley, C., 1994. Light and water radiative transfer in natural waters. Academic press, pp. 592.

Neckel, H. and Labs, D., 1981. Improved data for Solar Spectral Irradiance from 0.33 to 1.25 micrometres Solar Physics, 74: 231-249.

Onderka, M. and Pekárová, P., 2008. Retrieval of suspended particulate matter concentrations in the Danube River from Landsat ETM data. Science of The Total Environment, 397(1-3): 238-243.

Östlund, C., Flink, P., Strömbeck, N., Pierson, D. and Lindell, T., 2001. Mapping of the water quality of Lake Erken, Sweden, from Imaging Spectrometry and Landsat Thematic Mapper. The Science of The Total Environment, 268(1-3): 139-154.

Pattiaratchi, C., Lavery, P., Wyllie, A. and Hick, P., 1994. Estimates of water quality in coastal waters using multi-date Landsat Thematic Mapper data. International Journal of Remote Sensing, 15: 1571-1584.

Petzold, T., 1977. Volume scattering functions for selected ocean waters. In: J. Tyler (Editor), Light in the Sea. Dowden, Hutchinson and Ross, Stroudsburg, Pa. USA, pp. 150-174.

Pope, R. and Fry, E., 1997. Absorption spectrum (380-700 nm) of pure sea water: II, Integrating cavity measurements. Applied Optics, 36: 24.

Ruddick, K.G., Ovidio, F. and Rijkeboer, M., 2000. Atmospheric Correction of SeaWiFS imagery for turbid coastal and inland waters. Applied Optics, 39(6): 897-912.

Salama, M.S., Dekker, A., Su, Z., Mannaerts, C.M. and Verhoef, W., 2009. Deriving inherent optical properties and associated inversion-uncertainties in Dutch Lakes. Hydrology and Earth Systems Sciences, 13: 1113-1121.

Salama, M.S., Monbaliu, J. and Coppin, P., 2004. Atmospheric correction of Advanced Very High Resolution Radiometer imagery. Taylor & Francis Ltd, pp. 1349-1355.

Salama, M.S. and Shen, F., 2009. Simultaneous atmospheric correction and quantification of suspended particulate matters from orbital and geostationary earth observation sensors. Estuarine, Coastal and Shelf Science, In Press, Uncorrected Proof.

Shafique, N.A., Autrey, B.C., Fulk, F. and Cormier, S.M., 2001. Hyperspectral narrow wavebands selection for optimizing water quality monitoring on the Great Miami River, Ohio. Journal of Spatial Hydrology, 1(1): 1-22.

Shrestha, D.P., Margate, D.E., Meer, F.V.D. and Anh, H.V., 2005. Analysis and classification of hyperspectral data for mapping land degradation: An application in southern Spain. International Journal of Applied Earth Observation, 7: 85-96.

Storey, J.C., Scaramuzza, P. and Schmidt, G., 2005. Landsat 7 scan line corrector-off gap filled product development, PECORA 16 Conference Proceedings, Sioux Falls, South Dakota, pp. 23-27.

Vignolo, A., Pochettino, A. and Cicerone, D., 2006. Water quality assessment using remote sensing techniques: Medrano Creek, Argentina. Journal of Environmental Management, 81(4): 429-433.

Viollier, M., Tanre, D. and Deschamps, P.Y., 1980. An algorithm for remote sensing of water color from space. Boundary Layer Meteorology, 18: 247-267.

Walsh, S.J., McCleary, A.L., Mena, C.F., Shao, Y., Tuttle, J.P., González, A. and Atkinson, R., 2008. QuickBird and Hyperion data analysis of an invasive plant species in the Galapagos Islands of Ecuador: Implications for control and land use management. Remote Sensing of Environment, 112(5): 1927-1941.

Wang, Y., Xia, H., Fu, J. and Sheng, G., 2004. Water quality change in reservoirs of Shenzhen, China: detection using LANDSAT/TM data. Science of The Total Environment, 328(1-3): 195-206.

Werdell, P.J. and Bailey, S.W., 2005. An improved in-situ bio-optical data set for ocean color algorithm development and satellite data product validation. Remote Sensing of Environment, 98(1): 122-140.

Zhou, X., 2009. Characterisation of the specific inherent optical properties of the Poyang Lake and quantification of water turbidity using remote sensing and a semi-analytical bio-optical inversion model for shallow waters. MSc Thesis, International Institute for Geo-information Science and Earth Observation.

Zilioli, E. and Brivio, P.A., 1997. The satellite derived optical information for the comparative assessment of lacustrine water quality. Science of The Total Environment, 196(3): 229-245.

APPENDICES

Table A1: TM and ETM spectral range, post-calibration dynamic ranges, and mean exoatmospheric solar irradiance ($ESUN_\lambda$) for Visible and NIR spectral range

TM (Qcalmin=1 and Qcalmax=255					
Band	**Spectral range**	**Centre wavelength**	**$LMIN_\lambda$**	**$LMAX_\lambda$**	**$ESUN_\lambda$**
Units	µm		W/ (m^2srµm)		W/ (m^2m)
1	0.452-0.518	0.485	-1.52	169	1983
2	0.528-0.609	0.569	-2.84	333	1796
3	0.629-0.693	0.660	-1.17	264	1536
4	0.776-0.904	0.840	-1.51	221	1031
ETM+ (Qcalmin=1 and Qcalmax=255					
1	0.452-0.514	0.483	-6.2	191.6	1997
2	0.519-0.601	0.560	-6.4	196.5	1812
3	0.631-0.692	0.662	-5.0	152.9	1533
4	0.772-0.898	0.835	-5.1	157.4	1039

Table A2: Landsat image acquisition dates, site, sensor type and solar zenith and azimuth angles.

Image date	Site	Sensor	Solar zenith (degrees)	Solar azimuth (degrees)
05-09-2000	Roxo reservoir	ETM	37.08	140.71
04-06-2001	Roxo reservoir	ETM	24.70	120.95
01-07-2002	Roxo reservoir	TM	27.74	113.35
15-10-2008	Poyang Lake	ETM	42.99	147.47

Table A3: Water leaving reflectance measurements corresponding to the first 3 Landsat bands on the Poyang Lake

Site	Coordinate		Water leaving reflectance		
	Lat	Long	Band 1(λ_1)	Band 2(λ_2)	Band 3(λ_3)
P1	29.256567	116.073833	0.070340996	0.11604145	0.09830311
P2	29.246567	116.088567	0.098785104	0.15749107	0.14660198
P3	29.237550	116.101217	0.077696691	0.12880639	0.12354841
P4	29.228417	116.125317	0.065606143	0.10973315	0.08337301
P5	29.219300	116.152683	0.073692557	0.12181269	0.09942599
P6	29.209767	116.189550	0.073777562	0.12800010	0.94030060
P7	29.200828	116.191000	0.067506633	0.11331949	0.09869136
P8	29.191683	116.191683	0.099701905	0.15341649	0.13483435
P9	29.184417	116.197833	0.107174836	0.16462826	0.14398797
P10	29.175733	116.200150	0.116586492	0.18476651	0.15882522
P11	29.188967	116.210167	0.103325041	0.18677518	0.13724832
P12	29.199683	116.214944	0.057119870	0.09297714	0.07073056
P13	29.209400	116.212083	0.213983827	0.33249009	0.27232007
P14	29.221167	116.190883	0.108814587	0.15716639	0.13064441
P15	29.221128	116.200767	0.103220548	0.16171676	0.15013170
P16	29.392600	116.029367	0.078863408	0.11000719	0.09964310
P17	29.383617	116.041483	0.089565690	0.12594636	0.12289666
P18	29.374467	116.052883	0.074019516	0.12333918	0.10412255
P19	29.366050	116.059617	0.073341462	0.11837045	0.09810405
P20	29.356167	116.063850	0.103081229	0.14385528	0.12061243
P21	29.346167	116.063833	0.074230538	0.11826354	0.08898563
P22	29.337433	116.062450	0.072983092	0.11675189	0.09387327
P23	29.333767	116.059283	0.074964098	0.11995241	0.08701817
P24	29.320117	116.055050	0.086785371	0.12651100	0.09863203
P25	29.310400	116.051500	0.066628196	0.11012241	0.08231733
P26	29.301167	116.048583	0.071953853	0.11831971	0.08682045
P27	29.291983	116.048067	0.090620901	0.13636120	0.10602485
P28	29.282967	116.054050	0.065921983	0.11537715	0.07624218
P29	29.274000	116.058017	0.079836522	0.13158657	0.11803132
P30	29.265133	116.062100	0.077529243	0.13422459	0.12173574

Table A4: Measured and derived values of water leaving reflectance corresponding to the first 3 Landsat bands on the Poyang Lake from macth up pixels

Match-up	Measured WLR			Derived WLR			Relative error (%)		
site	Band 1	Band 2	Band 3	Band 1	Band 2	Band 3	Band 1	Band 2	Band 3
P2	0.098785	0.157491	0.146602	0.096438	0.120339	0.097641	2.37597	23.58995	33.39722
P3	0.077697	0.128806	0.123548	0.096526	0.114406	0.092249	-24.2344	11.17987	25.33372
P4	0.065606	0.109733	0.083373	0.099449	0.120339	0.097641	-51.5849	-9.66512	-17.1134
P5	0.073693	0.121813	0.099426	0.10585	0.126994	0.109032	-43.6373	-4.25351	-9.66147
P6	0.073778	0.128	0.09403	0.091527	0.122507	0.098855	-24.058	4.291484	-5.13127
P7	0.067507	0.113319	0.098691	0.08457	0.102179	0.086857	-25.2766	9.831041	11.99128
P8	0.099702	0.153416	0.134834	0.10313	0.133289	0.125816	-3.43835	13.11951	6.688465
P11	0.103325	0.186775	0.137248	0.114063	0.134267	0.124602	-10.3924	28.11304	9.214189
P15	0.103221	0.161717	0.150132	0.102372	0.126271	0.103033	0.822073	21.91842	31.37159
P16	0.078863	0.110007	0.099643	0.099828	0.126994	0.109032	-26.5834	-15.4415	-9.42253
P17	0.089566	0.125946	0.122897	0.11114	0.134628	0.11921	-24.0877	-6.89312	2.999808
P19	0.073341	0.11837	0.098104	0.102927	0.124209	0.10364	-40.3394	-4.93244	-5.64294
P20	0.103081	0.143855	0.120612	0.099828	0.123847	0.109032	3.155985	13.90862	9.601357
P23	0.074964	0.119952	0.087018	0.097373	0.118637	0.109639	-29.8928	1.096608	-25.9955
P25	0.066628	0.110122	0.082317	0.096438	0.117192	0.097641	-44.7405	-6.41976	-18.6154
P26	0.071954	0.11832	0.08682	0.079192	0.106772	0.082071	-10.0594	9.759752	5.470427
P27	0.090621	0.136361	0.106025	0.093515	0.117553	0.092249	-3.19363	13.79293	12.99304
P28	0.065922	0.115377	0.076242	0.093427	0.114045	0.097641	-41.7236	1.154603	-28.0669
P29	0.079837	0.131587	0.118031	0.090416	0.114045	0.097641	-13.2514	13.33082	17.27535
P30	0.077529	0.134225	0.121736	0.090972	0.111982	0.098248	-17.339	16.57117	19.29404

Table A5: Measured and derived values of Chla and SPM concentrations on the Poyang Lake from macth up pixels of Landsat

Match-up site	Measured		Derived		Relative error (%)	
	Chla(μg/l)	SPM(mg/l)	Chla(μg/l)	SPM(mg/l)	Chla	SPM
P2	1.416	19	0.334002	11.63716	76.40562	38.10021
P3	1.695	13	0.323162	11.45543	80.92877	14.69364
P4	0.808	13	0.328878	11.63716	59.29728	8.127676
P5	1.809	19	0.323357	16.32987	82.12312	12.51858
P6	3.496	14	0.347641	21.95118	90.05604	-56.7942
P7	0.430	13	0.31433	21.77682	26.96794	-64.9759
P8	0.933	32	0.325268	33.93555	65.14488	-4.73934
P11	1.384	35	0.311682	29.89683	77.48613	15.06582
P15	0.387	29	0.334696	17.94261	13.55992	38.83202
P16	1.193	32	0.333511	30.05551	72.03965	6.076537
P17	0.657	21	0.324083	15.19059	50.68731	28.34627
P19	0.301	30	0.326849	18.27681	-8.65991	38.25401
P20	0.152	25	0.324213	21.18043	-112.738	14.59505
P23	0.215	36	0.31258	24.53803	-45.311	31.83881
P25	1.189	22	0.32469	9.566318	72.68758	56.51674
P26	0.806	28	0.343006	11.45543	57.42229	58.49484
P27	0.808	28	0.337609	10.40442	58.19601	62.30284
P28	0.999	17	0.320555	14.25656	67.91884	16.13786
P29	0.385	26	0.325549	14.25656	15.48572	44.3103
P30	0.534	26	0.317917	16.39551	40.42035	37.89578